Functional redundancy of WDR31 with GTPase-activating proteins ELMOD and RP2 in regulating IFT trains via BBSome

Sebiha Cevik[1], Xiaoyu Peng[2], Tina Beyer[3], Mustafa S. Pir[1], Ferhan Yenisert[1], Franziska Woerz[4], Felix Hoffmann[3], Betul Altunkaynak[1], Betul Pir[1], Karsten Boldt[3], Asli Karaman[5], Miray Cakiroglu[5], S. Sadik Oner[4,5], Ying Cao[2], Marius Ueffing[3], Oktay I. Kaplan[1]†

1- Rare Disease Laboratory, School of Life and Natural Sciences, Abdullah Gul University, Kayseri, Turkey

2- School of Life Sciences and Technology, Tongji University, Shanghai 200092, China

3- Institute for Ophthalmic Research, Centre for Ophthalmology, University of Tuebingen, Elfriede-Aulhorn-Strasse 7, D-72076 Tuebingen, Germany.

4- Goztepe Prof. Dr. Suleyman Yalcin City Hospital, Istanbul, Turkey

5- Science and Advanced Technology Application and Research Center, Istanbul Medeniyet University, Istanbul

† Correspondence to oktay.kaplan@agu.edu.tr

Abstract

The correct intraflagellar transport (IFT) assembly at the ciliary base and the IFT turnaround at the ciliary tip are key for the IFT to perform its function, but we still have poor understanding about how these processes are regulated. Here, we identify WDR31 as a new ciliary protein, and analysis from zebrafish and *Caenorhabditis elegans* reveals the role of *WDR31* in regulating the cilia morphology. We find that loss of WDR-31 together with RP-2 and ELMD-1 (the sole ortholog ELMOD1-3) results in ciliary accumulations of IFT Complex B components and KIF17 kinesin, with fewer IFT/BBSome particles traveling along cilia in both anterograde and retrograde directions, suggesting that the IFT/BBSome entry into cilia and exit from cilia are impacted. Furthermore, anterograde IFT in the middle segment travel at increased speed in *wdr-31;rpi-2;elmd-1*. Remarkably, a non-ciliary protein leaks into cilia of *wdr-31;rpi-2;elmd-1* possible due to IFT defects. This work reveals WDR31-RP-2-ELMD-1 as IFT and BBSome trafficking regulators.

Introduction

Cilia are structurally and functionally distinct cellular projections, consisting of a microtubule-based axoneme extending from a centriole-derived basal body anchored at the plasma membrane. Cilia consist of multiple sub-compartments (basal body, transition zone, and ciliary tip) that display different protein compositions and structure (Blacque and Sanders, 2014; Rosenbaum and Witman, 2002; Satir and Christensen, 2007). Motile cilia mediate the movement of unicellular organisms such as *Chlamydomonas reinhardtii* or are involved in fluid movement across a tissue surface (Silflow and Lefebvre, 2001; Sleigh, 1989). Non-motile cilia, also known as primary cilia, possess mechanosensory, chemosensory, and osmosensory functions, and coordinate a range of extrinsic signaling pathways involved in cellular behavior, tissue development, and homeostasis such as those mediated by Hedgehog (Hh), Wnt, and receptor tyrosine kinase ligands (e.g. PDGFα) (Anvarian et al., 2019; Bloodgood, 2009; Nachury, 2014; Scholey, 2007).

The relation between cilia and human disorders has led to a greater understanding of their importance for human health. Both motile and primary cilia have been linked to the heterogeneous class of diseases known as ciliopathies, including Joubert Syndrome, Meckel Syndrome (MKS), and Nephronophthisis (NPHP). Owing to the presence of cilia on most cell types, ciliary defects result in varying multiorgan phenotypes such as kidney defects, retinitis pigmentosa, pancreatic cysts, hearing loss, congenital heart disease, and polydactyly (Reiter and Leroux, 2017; Wheway et al., 2019).

Over the last twenty years, there has been a large effort to reveal the molecular composition of cilia and its sub-compartments using several independent approaches, including clinical genomics, proteomics, functional genomics, and bioinformatics (Arnaiz et al., 2009; Avidor-Reiss et al.,

69 2004; Blacque et al., 2005; Breslow et al., 2018; Choksi et al., 2014; Jensen et al., 2016; Lambacher
70 et al., 2016; Li et al., 2004; Mick et al., 2015; Piasecki et al., 2010; Ruiz García et al., 2019;
71 Shaheen et al., 2016; Shamseldin et al., 2020; Sigg et al., 2017; UK10K Rare Diseases Group et
72 al., 2016; van Dam et al., 2019). Many proteins that make up the cilium, as well as many proteins
73 that regulate cilia biology, have been identified. These collective efforts have resulted in the
74 identification of 302 genes that are certain to be involved in cilia biogenesis, as well as over 180
75 ciliopathy genes. CiliaCarta estimates the total number of the ciliary genes to be about 1200 genes,
76 implying that many more ciliary proteins and ciliopathy genes are yet to be discovered. Indeed,
77 the genetic diagnosis of many ciliopathy disorders is still unknown (Shamseldin et al., 2020, 2020;
78 SYSCILIA Study Group et al., 2013; van Dam et al., 2019; Wheway et al., 2019).

79 Structural components of cilia and cilia cargos must be transported to cilia in order to construct
80 and sustain cilia, and mutations in genes involved in ciliary trafficking are commonly seen in
81 ciliopathies. Cilia has a one-of-a-kind protein delivery system called intraflagellar transport (IFT).
82 IFT is made up of multisubunit protein complexes that travel bidirectionally along the cilia. The
83 IFT complex contains two sub-complexes, IFT-A and IFT-B, consisting of 6 and 16 protein
84 subunits, respectively (Prevo et al., 2017). The IFT-B sub-complex and Kinesin-2 motors mediate
85 the motility of IFT and IFT cargos from the base of the cilia to the tip of the cilia (anterograde
86 IFT), while the IFT-A sub-complex and the cytoplasmic dynein-2 motor facilitate the retrograde
87 IFT transport (from the cilia tip to the base of the cilia) (Blacque, 2008; Rosenbaum and Witman,
88 2002). The IFT-A is involved in the transport of certain membrane proteins into cilia (Lee et al.,
89 2008; Liem et al., 2012; Mukhopadhyay et al., 2010). Mutations in genes encoding IFT
90 components lead to defects in cilia formation in all examined organisms, indicating the importance
91 of IFT for cilia assembly (Pazour et al., 2000; Prevo et al., 2017).

92 Bardet–Biedl syndrome (BBS) was classified as a ciliopathy in 2003, and eight of the highly
93 conserved Bardet-Biedl syndrome proteins (BBS1, BBS2, BBS4, BBS5, BBS7, BBS8, BBS9, and
94 BBIP10) establish a stable protein complex called the BBSome that undergoes IFT. Work from a
95 range of organisms implicates the BBSome in a variety of cilia related process including acting as
96 a cargo adaptor for removing proteins from cilia and as a regulator of the assembly and stability
97 of IFT trains (Ansley et al., 2003; Lechtreck et al., 2009; Loktev et al., 2008; Nachury et al., 2007;
98 Nozaki et al., 2019; Ou et al., 2007, 2005; Wei et al., 2012; Williams et al., 2014; Xu et al., 2015;
99 Ye et al., 2018). For example, in the nematode *C. elegans* mutants lacking *bbs-7* or *bbs-8*,
100 detachment of IFT-A and IFT-B in the amphid cilia was reported in the anterograde direction (Ou
101 et al., 2005). Analysis with a hypomorphic mutant (*bbs-1*) revealed that BBSome is involved in
102 attaching IFT-B components to the retrograde IFT machinery at the ciliary tips in the channel cilia
103 of *C. elegans* (Wei et al., 2012). Though it is known that the BBSome governs the IFT assembly
104 and returns of IFT from the cilia, we do not yet know which additional regulators control IFT
105 assembly at the ciliary base and IFT turnaround at the ciliary tip.

106 To identify new IFT regulators, we focused on our single-cell RNA-seq data that compared
107 expression profiles of ciliated cells with those of non-ciliated cells in the nematode *C. elegans,* and
108 this work revealed novel cilia genes and potential IFT regulators, including *WDR31* (manuscript
109 in preparation). Our gene discovery approach in combination with the use of *in vivo* IFT
110 microscopy analysis identified *WDR31* (WD repeat domain 31) and two GTPase activating
111 proteins (GAPs) as IFT regulators that facilitate the ciliary entry of IFT complex. Our work from
112 Zebrafish and *C. elegans* provides significant insight into the function of WDR31 in cilia
113 biogenesis. First, our work from *C. elegans* revealed that WDR-31 functions redundantly with two
114 GTPase activating proteins (GAPs) ELMD-1 (the sole ortholog of the human ELMOD proteins)

115 and RPI-2 (human retinitis pigmentosa 2 orthologue) to control the cilia morphology. Second,
116 knocking out *wdr-31* along with *elmd-1* or *elmd-1;rpi-2* causes IFT trafficking to be disrupted,
117 resulting in ciliary tip accumulations of IFT-B components and the OSM-3/KIF17 motor, as well
118 as significantly reduced BBSome recruitment to cilia. Third, fewer IFT/BBSome particles travel
119 along cilia in both anterograde and retrograde directions in *wdr-31;rpi-2;elmd-1* triple mutants,
120 indicating that the IFT/BBSome entry into and exit from cilia is affected. Third, anterograde IFT
121 in the middle segment moves faster in *wdr-31;rpi-2;elmd-1*. Finally, TRAM-1, a non-ciliary
122 membrane protein, penetrates *wdr-31;rpi-2;elmd-1* cilia. Taken together, this work identifies
123 WDR31 and two GAP proteins (ELMOD and RP2) as regulators for IFT and BBSome trafficking.

124 **Material and Methods**

125 ***C. elegans* strains, maintenance and genetic crossing**

126 For strain maintenance and genetic crosses, a standard procedure was followed, as described by
127 Sidney Brenner in 1974 (Brenner, 1974). After genetic cross with a marker to generate single,
128 double and triple mutants, we used the PCR strategy to trace the mutations in following mutants:
129 *wdr-31(T05A8.5)(tm10423)II.; wdr-31(tur003)II.; wdr-31(syb1568)II.; nphp-4(tm925)V.; mks-*
130 *6(gk674)I.; elmd-1(syb630) III.; RB1550 rpi-2(K08D12.2)(ok1863) IV.*; and *bbs-8(nx77) V*.
131 Primers can be found in Table S1.

132

133 **Lipophilic fluorescent dye-uptake assay and rescue analysis**

134 Healthy mixed-staged animals were collected using M9 buffer (3 g/L KH2PO4, 6 g/L Na2HPO4,
135 5 g/L NaCl, 1 mM MgSO4), centrifuged for 1 minute at 2000 rpm, and washed twice with M9
136 buffer to remove any bacterial contaminations. Worms were incubated for 45-60 minutes at room
137 temperature in an M9 buffer containing lipophilic dye (1:200 dilution in M9, Invitrogen™

138 Vybrant™ DiI Cell-Labeling Solution) (Herman and Hedgecock, 1990). The worms were then
139 washed twice with M9 before being moved to a new NGM plate. Wild type was always included
140 in Dye filling assay, and the dye uptake control for the wild type was performed under a stereotype
141 fluorescence microscope, followed by imaging with the fluorescence upright microscope. For the
142 rescue experiment, *N2;turEx24[arl-13p::GFP::elmd-1 (C56G7.3)::unc-54 3'UTR +rol-6}*
143 (OIK1045) were crossed into *wdr-31(T05A8.5)(tm10423)II., elmd-1(syb630) II,* double and *wdr-*
144 *31(T05A8.5)(tm10423)II., elmd-1(syb630) II, rpi-2(K08D12.2)(ok1863) IV.* triple mutants.
145 *N2;turEx21[arl-13p::wdr-31 (T05A8.5)::GFP::unc-54 3'UTR +rol-6} (1 ng)* (OIK1042) were
146 mated with *T05A8.5(syb1568)II., elmd-1(syb630) II, rpi-2(K08D12.2)(ok1863) IV.* triple mutants.
147 Plasmid (*arl-13p::wdr-31 (T05A8.5)::GFP::unc-54 3'UTR*) was directly microinjected into triple
148 mutant *T05A8.5(syb1568)II., elmd-1(syb630) II, rpi-2(K08D12.2)(ok1863) IV* (1 ng). *dpy-*
149 *5(e907);nxEx386[rpi-2::gfp + dpy-5(+)]* (MX352) were crossed into *wdr-*
150 *31(T05A8.5)(tm10423)II., elmd-1(syb630) II, rpi-2(K08D12.2)(ok1863) IV.* triple mutants. Three
151 independent Dye uptake assays were performed, and fluorescence filters were set for GFP and
152 Texas Red, followed by fluorescence imaging (20-150 heads and tails were counted). Dye uptake
153 of mutants with corresponding transgenics strains was compared to that of non-transgenic strains
154 in the same rescue plates **(Fig. S2C, D)**.
155

156 **Generation of mutants using CRISPR/Cas9 in the nematode *Caenorhabditis elegans***

157 To generate *wdr-31(T05A8.5)(tur003)* allele, three sgRNAs targeting *C. elegans* T05A8.5 (human
158 WDR-31) were chosen using an online tool, Benchling [Biology Software] (2019), followed by
159 ordering complementary oligonucleotides (Macrogen, South Korea), and cloning of sgRNAs into
160 an empty sgRNA vector pRB1017. The successful sgRNA insert was confirmed with colony PCR,

161 followed by plasmid isolation. Three sgRNAs (each 50 ng/µl) were injected into the gonads of
162 wild type together with pDD162 (*Peft-3::Cas9;* 15 ng/ µl plasmid pRF4) and pRF4 (50 ng/ µl
163 plasmid pRF4) (Dickinson et al., 2013). F1s with the roller phenotype were identified, and after
164 they generated enough progenies, the PCR technique was used to identify the F1 generation
165 bearing the predicted deletion, as well as the homozygosity of the allele mutation. The PCR
166 products from knockout animals were then sent to the Sanger sequencing (Macrogen, South
167 Korea). *wdr-31(*tur003*)II.* mutants have 1276-bp deletion covering a huge part of exon II (297 bp
168 out of 359 bp) and whole exon III, IV, and exon V. This is likely a null allele of *wdr-31.* sgRNA
169 sequences can be found in Table S1.
170

171 **Generation of transgenic strains and strain list for *C. elegans***

172 To generate transgenic lines for localization, rescue experiments, and expression patterns, we
173 generated the following transgenic animals via microinjections.

174 *OIK1042 turEx21[arl-13p::wdr-31 (T05A8.5)::GFP::unc-54 3'UTR +rol-6}*;
175 *T05A8.5(syb1568)II., elmd-1(syb630) II, rpi-2(K08D12.2)(ok1863) IV.* (1 ng)

176 *OIK1044 N2;turEx23[elmd-1p::GFP::elmd-1 (C56G7.3)::unc-54 3'UTR +rol-6}* (5 ng)

177 *OIK1045 N2;turEx24[arl-13p::GFP::elmd-1 (C56G7.3)::unc-54 3'UTR +rol-6}* (5 ng)

178 *OIK1046 N2;turEx25[elmd-1p(C56G7.3)::GFP::unc-54 3'UTR +rol-6}* (50 ng)

179 *OIK1047 N2;turEx26[wdr-31 (T05A8.5)p::GFP::unc-54 3'UTR +rol-6}* (50 ng)

180 The rol-6 plasmid (50 ng/ µl plasmid pRF4) was co-injected as the co-transformation marker. In
181 brief, the plasmids were delivered by microinjections into the gonads of 1-day adult worms.
182 Worms were initially transferred onto a 2.5% agarose pad prior (Halocarbon oil, Sigma: 9002-83-
183 9), followed by microinjection. The microinjection was done using a Zeiss Axio Vert.A1 inverted

184 microscope with DIC optics coupled with a Narishige Micromanipulator MMO-4. We next
185 manually inspected the plates to find successful transgenics animals.
186 **Wild Type and mutant alleles:** N2; *FX30333; wdr-31*(*T05A8.5)(tm10423)II.; OIK393*
187 *T05A8.5(tur003)II.; PHX1568 T05A8.5(syb1568)II.; nphp-4(tm925)V.; mks-6(gk674)I.;*
188 *PHX630, elmd-1(syb630) III.; RB1550 rpi-2(K08D12.2)(ok1863) IV.*; *MX52, bbs-8(nx77) V.* We
189 obtained *wdr-31(T05A8.5)(tm10423)II. (FX30333)* mutant allele, which has a 160-bp deletion,
190 causing a frameshift, from the National Bioresource Project, Japan. The *wdr-*
191 *31(T05A8.5)(tm10423)II.* were outcrossed to wild type four times. The Caenorhabditis Genetics
192 Center (CGC), Minnesota, USA, provided the *RB1550 rpi-2(K08D12.2)(ok1863)* mutant, and the
193 *rpi-2(ok1863)* allele contains 1143-bp deletion that removes a large segment of exon III, exon IV,
194 and some portion of exon V. *T05A8.5(syb1568)II.* has 1888-bp deletion, deleting all exons except
195 exon I **(Supplementary Fig. 3B)**. Sunybiotech created an independent null allele of *elmd-1* via
196 CRISPR–Cas9. The *PHX630, elmd-1(syb630) III.* mutant contains 1784-bp deletion, where except
197 for exon I, all exons were removed **(Supplementary Fig. 2B)**. *elmd-1(syb630) III.* were outcrossed
198 to wild type two times.
199
200 **Fluorescent transgenes for IFT proteins:** *GOU2162 che-3(cas443[gfp::che-3]) I; xbx-*
201 *1(cas502[xbx-1::tagRFP]) V ; GOU2362 ift-74(cas499[ift-74::gfp]) II.; EJP76 vuaSi15*
202 *[pBP36; Posm-6::osm-6::eGFP; cb-unc119(+)] I; unc-119(ed3) III; osm-6(p811) V;*
203 *N2;lqIs2[osm-6::gfp], N2;ejEx[osm-3::GFP + pRF4]; N2;ejEx[kap-1::gfp+pRF4]; EJP81*
204 *vuaSi24 [pBP43; Pift-140::ift-140::mCherry; cb-unc-119(+)]II; unc-119(ed3) III; ift-*
205 *140(tm3433) V; jhuEx [ift-140::GFP+pRF4]; Ex[rpi-2::GFP+ xbx-1::tdTomato+pRF4]; MX76*
206 *dpy-5(e907); nxEx(bbs-7::gfp+dpy-5 (+)).*

207 **Fluorescent transgenes for ciliary proteins:** PHX1180, *wdr-31(syb1180 [wdr-*
208 *31(T05A8.5)::GFP]); PHX4934 rpi-2(syb4934) [rpi-2::mCherry]; OIK1042 N2;turEx21[arl-*
209 *13p::wdr-31 (T05A8.5)::GFP::unc-54 3'UTR +rol-6} (5 ng); OIK1044 N2;turEx23[elmd-*
210 *1p::GFP::elmd-1 (C56G7.3)::unc-54 3'UTR +rol-6} (5 ng); OIK1045 N2;turEx24[arl-*
211 *13p::GFP::elmd-1 (C56G7.3)::unc-54 3'UTR +rol-6} (5 ng); OIK1046 N2;turEx25[elmd-*
212 *1p(C56G7.3)::GFP::unc-54 3'UTR +rol-6} (50 ng); OIK1047 N2;turEx26[wdr-31*
213 *(T05A8.5)p::GFP::unc-54 3'UTR +rol-6} (50 ng)*; *N2;Ex[mks-2::GFP + tram-1::tdTOMATO +*
214 *pRF4]; MX1409 N2; nxEx785[tax-4:gfp+ Posm-5::xbx-1::tdTomato + rol-6(su1006)];*
215 *vuaSi21[pBP39; Pmks-6::mks-6::mCherry; cb-unc-119(+)]II; MX2418 N2;nxEx1259[pbbs-*
216 *8::PLC-delta PH::GFP;MKSR-2::tdTomato; coel::GFP]; PY8847 oyIs65[str-1p::mcherry];*
217 *Ex[str-1p::nphp-4::gfp, unc122p::dsRed]*. All PHX strains were generated using CRISPR/Cas9
218 by Sunybiotech. The list of extensive transgenic and mutant strains was provided in Table S2.
219

220 **Fluorescence and Confocal microscopy for *C. elegans***

221 Fluorescence images (dye assay) and time-lapse movies (IFT movies) were captured using an epi-
222 fluorescence upright microscope (Leica DM6 B) (3 frames per second, and up to 120 frames). The
223 epi-fluorescence upright microscope was controlled with iQ3.6.2 Andor software and was attached
224 with an Andor iXon Ultra 897 EMCCD (an electron-multiplying charge-coupled device camera).
225 The LSM900 confocal microscope with Airyscan 2 (ZEN 3 Blue edition software) was used to
226 capture the high-resolution Z-stack images. On microscope slides, a drop of 2-3% agarose was
227 used to create an agarose pad, and worms were then moved to the agarose pad containing 1-3 µl
228 of 10 mM levamisole (an anesthetic agent). Images were collected at 0.14 m intervals with a Plan

229 ApoChromat 63x/1.40 NA target, then analyzed with Blue edition software ZEN 3 to create Z-
230 stacks, and processed with ImageJ (NIH) software (Schneider et al., 2012).

231 ***In vivo* intraflagellar transport assay for IFT frequency and velocity**

232 The time-lapse movies of GFP-labelled IFT proteins were analyzed with the automatic kymograph
233 analyzing tools KymographClear and KymographDirect, both of which are ImageJ based
234 (Mangeol et al., 2016; Turan et al., 2022). KymographClear was used to produce kymographs from
235 time-lapse movies. We examined each produced kymograph and calculated IFT frequency or IFT
236 velocities for IFT-74::GFP (an endogenously tagged), GFP::CHE-3 (an endogenously tagged),
237 BBS-7::GFP (an overexpression transgene), OSM-6::GFP (a single copy transgene), OSM-3::GFP
238 (an overexpression transgene), and IFT-140::GFP (an overexpression transgen) in wild type, *wdr-*
239 *31;elmd-1* double and *wdr-31;elmd-1;rpi-2* triple mutants. All worms were maintained at 20 °C
240 for IFT analysis. At least ten IFT videos were taken over three separate time periods for strains,
241 and IFT particles from at least ten kymographs were counted.

242 **Whole-mount *in situ* hybridization in zebrafish**

243 Whole-mount in situ hybridization was performed as previously described (Thisse et al., 2004).
244 The *wdr31* cDNA with T7 promoter was PCR amplified, with forward primer:
245 ATGGGGAAGCTACAGAGCAAGTTC and reverse primer:
246 TAATACGACTCACTATAGAAGCGAGCCACTTCAGTGATACTG, from a homemade
247 cDNA library of zebrafish embryos at 24 hpf. The antisense probe for *wdr31* was then transcribed
248 with digoxigenin-labeled UTPs and T7 RNA polymerases (Roche, Basel, Switzerland). The
249 stained embryos were dehydrated in glycerol and photographed with a Nikon SMZ1500
250 stereomicroscope (Nikon, Tokyo, Japan).

251

252 **Mutagenesis of *wdr31* in zebrafish using the CRISPR/Cas9 technology**

253 Generation of zebrafish mutants using the CRISPR/Cas9 system was carried out as previously
254 described (Chang et al., 2013). Briefly, two gRNAs targeting sequences in *wdr31* were chosen as
255 following: 5'- ACCCATGTGTGTTGGGTACC-3' and 5'-GAAGCCATCCAGGAGTTCAG-3'.
256 gRNA templates were PCR amplified and gRNAs were *in vitro* transcribed with T7 transcriptase
257 (NEB, cat# M0251S). gRNAs and Cas9 protein (NEB, cat# M0251S) were simultaneously injected
258 into the embryos at one-cell stage.
259

260 **Immunofluorescence staining and microscopy**

261 Immunostaining was performed as previously described (Xu et al., 2017). Briefly, embryos were
262 fixed in cold Dent's fixative (80% methanol: 20% dimethyl sulfoxide) at -20°C overnight and then
263 stored in methanol. Samples were permeabilized with 0.005% (m/v) trypsin for 30 minutes.
264 Samples were blocked with blocking buffer (10% [v/v] goat serum in PBST), followed by
265 incubation with primary antibody anti–acetylated tubulin (1:2000; Sigma-Aldrich, St. Louis, MO)
266 and then secondary antibodies conjugated with Alexa Fluor 568 (1:500; Invitrogen, Carlsbad, CA).
267 Samples were mounted on ProLong Gold Antifade Mountant with DAPI (Invitrogen) and images
268 were taken with a Nikon A1R confocal microscope.
269

270 **Software and algorithms**

271	Zen Blue	Zeiss	https://www.zeiss.com/corporate/int/home.html
272	Andor iQ3	Andor	https://andor.oxinst.com/
273	Fiji	ImageJ	https://fiji.sc
274	ImageJ	ImageJ	https://imagej.nih.gov/ij/
275	Illustrator (CS5.1)	Adobe, USA	https://www.adobe.com/
276	KymographClear	Peterman Lab	https://sites.google.com/site/kymographanalysis

277 R R Core Team https://www.r-project.org/

278

279 **Statistical analysis and Generating Figures**

280 For statistical analysis of dye assay, Fisher's exact test (one tailed tests) was performed. For data
281 involving continuous variables like IFT speed and cilia length, Mann-Whitney U-test or Welch's
282 t-test was used depending on the distribution of data. Transgenic worms were kept at 15 °C for
283 AWB cilia morphology analysis and AWB cilia length measurements, and only L4 stage animals
284 were imaged for AWB cilia. For each strain, at least three independent microcopy analyses were
285 performed, and 60-220 AWB cilia were examined. All statistical tests were performed using R
286 software. The codes and files needed to generate figures and perform statistical analysis were
287 openly shared, and the files and codes for making figures and performing statistical analysis may
288 be accessed at https://github.com/thekaplanlab/WDR31-ELMOD-RP2.

289 **Gateway Cloning (mammalian constructs)**

290 Constructs for ELMOD3 (HsCD00288286) and WDR31 (HsCD00045652) were purchased
291 from Harvard Medical School. LR Reaction (Invitrogen, USA) was performed to transfer the target
292 sequence into destination vectors ((N)RFP, (N)CFP plasmids) with a subsequent transformation
293 into *E. coli* DH5α. DNA was isolated according to Monarch® Plasmid Miniprep Kit (BioLabs,
294 USA) and the PureYield® Plasmid Midiprep Protocol System (Promega, USA). Verification of
295 successful cloning was done by sequencing (Eurofins, Luxembourg).

296

297 **Immunofluorescence Staining (Mammals)**

298 hTERT-RPE1 cells were transiently transfected according to Lipofectamine™ 3000 Reagent
299 Protocol with ELMOD3-CFP and WDR31-RFP constructs followed by serum starvation for three

300 days to induce cilia formation. Cells were fixed with 4% PFA for 45min at 4°C, permeabilized for
301 5min with 0.3% PBST and blocked with 10% goat serum in PBST at 4°C overnight. A primary
302 antibody for ARL13B (1:50; Proteintech, Germany) and a secondary antibody conjugated to Alexa
303 Fluor 647 (1:350; Invitrogen, USA) were used. Cells were mounted using Fluoromount-G
304 (Invitrogen, USA).

305 **Microscopy Setup (Mammals)**

306 Images were captured using a Leica TCS SP8 scanning microscope (Leica Microsystems IR
307 GmbH, Germany). The setup includes 488 nm, 532 nm and 635 nm pulsed excitation lasers as
308 well as 100x oil immersion objective lens (NA 1.4) and a hybrid detector (HyD). Pixel number
309 was 1024 x 1024 and optimal pixel size was determined by Nyquist calculation resulting in a size
310 of 43 × 43 nm in XY. Additionally, Z-steps should not exceed 131 nm when acquiring a stack.
311 Laser intensity was adjusted for each sample and images were recorded with 2x frame averaging.

312 **Image Processing (Mammals)**

313 Acquired images were processed (LasX, Leica Microsystems), deconvoluted (Huygens Software,
314 SVI, Netherlands) and edited (FIJI software). The deconvolution was performed with a Classical
315 Maximum Likelihood Estimation (CMLE) algorithm under experimentally defined settings. The
316 background level was software estimated, the quality threshold was 0.001, the number of iterations
317 was 50 and signal-to-noise ratio was set to 20. All images were brightness-corrected for the
318 purpose of presentation.

319

320 **Results**

321 **WDR31 and ELMOD are evolutionarily conserved constituents of cilia**

322 As part of our ongoing effort to reveal novel cilia genes, using single-cell RNA-seq data, we
323 conducted comparative expression analysis in *C. elegans* and discovered that the WDR31 and
324 ELMOD orthologues, WDR-31 (T05A8.5) and ELMD-1 (C56G7.3), are likely expressed
325 exclusively in ciliated sensory neurons (manuscript in preparation). The head (amphid) and tails
326 (phasmid) of *C. elegans* contain a total of 60 ciliated sensory neurons, and the expression patterns
327 of genes can be reliably analyzed using fluorescence tagged promoter markers. Consistent with
328 our predictions, promoter-based GFP reporters revealed that both WDR-31 and ELMD-1 are
329 expressed in most of the ciliated sensory neurons **(Fig. S1A)**. To explore if both proteins are
330 concentrated within cilia, we investigated their subcellular localization in *C. elegans* and created
331 CRISPR/Cas9-mediated knock-in of WDR-31::GFP and a transgenic animal expressing GFP-
332 tagged ELMD-1. The endogenously expressed WDR-31::GFP is concentrated at the ciliary base
333 in both head and tails, where it colocalizes with the basal body marker γ-tubulin (TBG-1, the
334 ortholog of human TUBG1), and the IFT-140 (human IFT140) basal body signal **(Fig. 1A, B, C,**
335 **and D)**, so our co-localization data suggests that WDR-31 is a new cilia-associated protein.
336 ELMD-1 is the sole orthologue of the three human ELMOD proteins (ELMOD1-3) that function
337 as GTPase-activating proteins (GAP). We found that GFP::ELMD-1 localizes to the periciliary
338 membrane compartment (PCMC) and the basal body (BB) (marked with IFT-140), but is proximal
339 to the MKS-6-labeled transition zone that is adjacent to the BB **(Fig. 1E, F, and G)** (Kaplan et al.,
340 2012).
341
342 To determine if both human WDR31 and ELMOD3 (also known RBED1, the top blastp hit for
343 *elmd-1*) are concentrated within cilia in mammalian cell lines, we generated hTERT-RPE1 cells
344 co-expressing WDR31-RFP and ELMOD3-CFP and stained them with a ciliary marker ARL13B.
345 Furthermore, WDR31-RFP or ELMOD3-CFP were transiently transfected into hTERT-RPE1

346 cells, and they were additionally stained for ARL13B. Our super-resolution microscopy analysis
347 revealed that both WDR31 and ELMOD3 are enriched in the cilium **(Fig. 2A, B and Fig. S2B**
348 **and C)**. Taken together, our complementary approach demonstrates that both WDR31 and
349 ELMOD3 are evolutionarily conserved proteins associated with cilia.
350
351 **Wdr31 regulates ciliogenesis in the Zebrafish ear**
352 We turned our interest into zebrafish to develop an *in vivo* model for WDR31 to examine the role
353 of WDR31. We first used the whole-mount *in situ* hybridization (ISH) within zebrafish to visualize
354 the expression pattern of *wdr31* during zebrafish embryo development up to 1-day post-
355 fertilization. The dynamic and wide expression of *wdr31* during zebrafish embryonic development
356 (2 cell and 8 somite stages (SS)) has become restricted to the otic vesicle and brain region at 24
357 hours post-fertilization (24 hpf) **(Fig. 3A)**. We next knocked out (KO) *wdr31* in zebrafish with the
358 CRISPR/Cas9 system and the embryos showed heart edema and otolith malformation. As *wdr31*
359 is expressed in the otic vesicle and the otolith development requires cilia, we checked the cilia in
360 the otic vesicle. The cilia bundle in the lateral crista (LC) of the otic vesicle was stained with
361 acetylated tubulin in wild type and *wdr31* KO, and although we found that the length of LC cilia
362 was comparable with wild type, the width of the cilia bundle was reduced by 33% in LC of the
363 otic vesicle compared to that in the control embryos, suggesting the cilia number is decreased **(Fig.**
364 **3B, C, and D).** Our zebrafish work indicates that WDR31 plays a role in ciliogenesis in the
365 zebrafish ear.
366
367 **Functional redundancy of WDR31, ELMOD, and RP2 for determining cilia morphology**
368 We next wanted to gain mechanistic insight into the functions of *wdr-31* in cilia biogenesis. To
369 this end, we employed the nematode *C. elegans* and obtained/generated three *wdr-31* alleles:

370 tm10423 (160-bp frameshift causing deletion), syb1568 (1888-bp deletion removing all exons
371 except exon I), and tur003 (1276-bp deletion removing a large portion of exon II and exon III, IV,
372 and exon V) (**Fig. S3B)**. In *C. elegans,* the lipophilic fluorescent dye-uptake assay is employed to
373 indirectly evaluate the cilia structure, and our analysis revealed *wdr-31* mutants display wild type
374 level dye-uptake in both head (amphid) and tail (phasmid), suggesting cilia structures are likely
375 unaffected in these mutants **(Fig. 4B and Fig. S4A)**. To address whether loss of *wdr-31* leads to
376 subtle defects in cilia morphology, we expressed the fluorescence-based marker *str-1pro:mCherry,*
377 *gcy-5pro::gfp, srb-6pro::gfp ,* which label the AWB, ASER and PHA/PHB cilia, respectively, in
378 *wdr-31* mutants. The AWB dendritic tip extends the fork-like cilia in the wild type, and rod-like
379 cilia protrude from the dendritic endings of ASER and PHA/PHB sensory neurons. Our confocal
380 microscopy analysis revealed that the structure and length of ASER, PHA/PHB, and AWB cilia
381 are comparable with those of wild type cilia, suggesting, contrary to the importance of WDR31
382 for ciliogenesis in the zebrafish ear, the loss of *wdr-31* alone does not result in a severe defect in
383 cilia structure **(Fig. 4C, D, E, F, and G)**.

384 The lack of an apparent cilia phenotype in *C. elegans* may be attributed to a functional
385 redundancy for WDR-31 in cilia biogenesis, and functional redundancy is indeed a common
386 phenomenon in ciliopathy-related genes. For example, while the absence of individual ciliopathy
387 genes encoding MKS/MKSR proteins or NPHP proteins (NPHP-1, NPHP-4) does not result in
388 serious cilia defect, the loss of *nphp-4* (the ortholog of human NPHP4) in combination with *mks-*
389 *6* (the ortholog of human CC2D2A) causes more severe cilia related defects (transition zone
390 membrane association defects) (Williams et al., 2011). We next explored genetic interaction
391 between *wdr-31* and *elmd-1*, since our results showed that both protein products are at the ciliary
392 base **(Fig. 1C, D, E, and F)**. We discovered that the *wdr-31(tm10423);elmd-1(syb603)* double

393 mutant (hereinafter referred to as "double mutant") has a partial Dyf defect in both head and tail
394 neurons, which was rescued by expression of a transgene containing the wild type *elmd-1* sequence
395 **(Fig. 5B and Fig. S4A,** $p < 0.0001$, Fisher's exact test**)**. Using the AWB, ASER and PHA/PHB
396 cilia fluorescence markers, we subsequently set out to visualize the ciliary structures in the double
397 mutant and single mutants. The AWB cilia in the double mutants have an extra projection in the
398 middle part of the cilia (7% (N: 100) and 52 % (N: 134) in WT and double mutant, respectively),
399 whereas ASER, AWB, and PHA/PHB cilia are normal length in WT and double mutant **(Fig. 4C**
400 **and D, E, and F and Fig. S4B)**.

401 We explored genetic interaction between *wdr-31, elmd-1,* and *rpi-2* (the X-linked retinitis
402 pigmentosa protein RP2 and a GTPase-activating protein) since ELMD-1 and WDR-31
403 localizations are reminiscent of RPI-2 localization (the endogenously labeled RPI-2) in *C. elegans*
404 (**Fig. 4A, and Fig. S5A)** (Williams et al., 2011). We, therefore, first generated an *elmd-1;rpi-2*
405 double mutant, which revealed no Dyf phenotype **(Fig. 4B, and Fig. S4A)**. However, when we
406 created *wdr-31;elmd-1;rpi-2* triple mutants (hereinafter referred to as "triple mutant"), we
407 observed severe synthetic Dyf phenotype, which is significantly rescued by the introduction of a
408 wild-type copy of *wdr-31* or *elmd-1 or rpi-2* **(Fig. 4B, Fig. S3C, and Fig. S4A** $p < 0.0001$, Fisher's
409 exact test**)**.

410 We then sought to examine AWB, ASER and PHA/PHB cilia morphology in triple mutants
411 and compared them with the *wdr-31;elmd-1* and *rpi-2;elmd-1* double mutants. The Dyf defect of
412 triple mutants was indeed accompanied by significant changes in these cilia. The AWB cilia
413 displayed the ectopic projections, including a backward projection from the base of AWB cilia in
414 triple mutant and as wells as ectopic projections from the middle part of AWB cilia (0% backward
415 projection in wild type vs over 30% backward projection in triple mutant; $p < 0.0001$, Fisher's

416 exact test) (**Fig. 4F and G**). It is noteworthy that the similar backward projections in AWB cilia
417 were observed in two independent triple mutants generated with *wdr-31(syb1568)* and *wdr-*
418 *31(tur003)* (**Fig. S7A and B**). A backward projection from the ciliary base was observed for ASER
419 cilia, but not PHA/PHB cilia in triple mutants (**Fig. 4F)**. We next measured the cilia lengths of
420 these cilia and discovered that ASER and PHA/PHB cilia are significantly shorter in triple mutants
421 (20% shorter for ASER in triple mutants, 13% shorter for PHA/PHB in triple mutants), whereas
422 the cilia length of AWB cilia was not significantly altered in triple mutants **(Fig. 4C, D, F, and**
423 **Fig. S4B)**. This establishes a role for WDR-31 in controlling cilia length and morphology in a
424 subset of sensory neurons in a redundant manner with RPI-2 and ELMD-1.
425
426 **WDR-31-ELMD-1-RPI-2 are needed for effective cilia entry and exit of IFT components.**
427 We next aimed to investigate the mechanism by which WDR-31, ELMD-1, and RPI-2 regulate
428 cilia morphology in *C. elegans.* To this end, we investigated whether these genes affect the
429 localization of IFT proteins and IFT motors, including kinesin motors (Kinesin II and OSM-
430 3/KIF17), dyneins, and IFT components (IFT-A and IFT-B). The IFT complex and motor proteins
431 are critical for cilia construction and maintenance because they deliver ciliary constituents from
432 the cell body to the cilia. In *C. elegans,* two kinesin motors Kinesin II and OSM-3/KIF17
433 (heterotrimeric kinesin-II and homodimeric OSM-3) work cooperatively to carry the IFT complex
434 in the middle segment of the channel cilia in an anterograde direction, while OSM-3/KIF17
435 transports the entire IFT complex (IFT-A, IFT-B, and BBSome) in the distal part of channel cilia.
436 We generated single, double, and triple mutants expressing fluorescence tagged IFT and
437 motor proteins. Using single-copy transgenes, we found that IFT-B components predominantly
438 accumulate at cilia tips and/or middle of cilia in double mutants (96% ciliary tip accumulations for
439 IFT-74/IFT74, N: 26 and 82% ciliary tip accumulations for OSM-6/IFT52, N: 46) but the

440 localization of GFP::CHE-3 (human dynein heavy chain DYNC2H1) remains less affected in
441 double mutants (27% minor middle cilia accumulations for CHE-3; N: 48, see supplementary
442 Movie S1) **(Fig. 5A, C and D and Supplementary Movie S1, 2, 4)**. Furthermore, we next
443 investigated the localization of GFP::CHE-3 in triple mutants because the cilia morphology of
444 triple mutants is more severe than that of *wdr-31;elmd-1* or *wdr-31;rpi-2* or *elmd-1;rpi-2* double
445 mutants (**Fig. 5A).** Compared with wild type and double mutants, we noticed additional IFT
446 abnormalities in two independent triple mutants, including dim cilia staining with GFP::CHE-3
447 and accumulations of GFP::CHE-3 in the middle/distal part of cilia (81% middle cilia
448 accumulations, N: 96; 6.6% ciliary tip accumulations, N: 90) (**Fig. 5A and Supplementary Movie**
449 **S1)**. Motor protein OSM-3/KIF17 accumulation within the ciliary tips was detected in double and
450 triple mutants **(Fig. 5B, and Supplementary Movie S3)**. Furthermore, in triple mutants, the dim
451 distal cilia staining was observed for IFT-140::GFP (IFT-A component) (63% dim distal cilia, N:
452 47) and XBX-1::mCherry (a dynein light intermediate chain) **(Fig. 5E and F and Supplementary**
453 **Movie S5)**, but the ciliary distribution of KAP-1::GFP (Kinesin II) remains unaffected **(Fig. 5G)**.
454
455 Cilia accumulations of IFT-B components and OSM-3/KIF17 coupled with weak cilia
456 staining with IFT-A components in triple mutants forced us to better understand the role of WDR-
457 31-ELMD-1-RPI-2 in IFT defects, we therefore employed *in vivo* time-lapse video coupled with
458 kymography. For a subset of IFT components, we detected a significant decline in the quantity of
459 IFT particles traveling along the cilia in both directions in double and triple mutants (**Figure 6A,**
460 **B, C, D, E, E, G, and H**). We found significant decline in the IFT transport for kinesin motor
461 OSM-3::GFP in double and triple mutants in both anterograde and retrograde directions (the
462 anterograde and retrograde: 0.68 n/s and 0.61 n/s in wild type; 0.43 n/s and 0.32 n/s in double
463 mutants; 0.34 n/s and 0.23 n/s in triple mutants, $p < 0.0001$; the Mann–Whitney U test) (**Fig. 6A,**

464 **and B**), while our analysis revealed that the flux of cytoplasmic dynein motor protein CHE-3 along
465 the cilium was unchanged in both directions in both double and triple mutants (**data not shown**),
466 suggesting, indicating that the simultaneous elimination of these genes has an effect on the kinesin
467 motor OSM-3 but not on cytoplasmic dynein loading onto IFT, but their absence leads to both
468 ciliary cytoplasmic dynein accumulation and the kinesin motor OSM-3 (**Fig. 5A and B**). In wild
469 type, the average of IFT-74 particles moving in anterograde and retrograde directions is 0.58 (n/s:
470 number of particles/seconds) and 0.52 n/s, respectively, while in triple mutants, the anterograde
471 and retrograde IFT-74 particles are 0.27 n/s and 0.09 n/s. Comparable reductions were observed
472 for IFT-74::GFP (CRISPR tagged endogenous IFT-74) in *wdr-31;eldm-1* double mutant (0.36 n/s
473 and 0.21 n/s in *wdr-31;eldm-1;* $p < 0.0001$; the Mann–Whitney U test) (**Fig. 6G, and H**). For
474 OSM-6::GFP, the anterograde and retrograde IFT particles statistically differ between wild type
475 and triple mutants (the anterograde and retrograde: 0.52 n/s and 0.58 n/s in wild type, 0.36 and
476 0.30 in triple mutants*;* $p < 0.0001$; the Mann–Whitney U test) (**Fig. 6E, and F**). Furthermore, IFT-
477 A component IFT-140 transport declined in both directions both double and triple mutants (**Fig.**
478 **6C, and D**). Taken together, our fluorescent microscopy analysis reveals several IFT abnormalities
479 in triple mutants: first, in triple mutants, there is a significant decrease in the quantity of IFT
480 particles, including the OSM-3/KIF17 kinesin motor and both IFT-A and IFT-B components,
481 traveling in both anterograde and retrograde directions. Second, the ciliary accumulations of IFT-
482 B components and OSM-3/KIF17 kinesin motors in cilia together with weak distal cilia staining
483 of the IFT-A component and dynein (XBX-1) in triple mutants suggest that the defects in the return
484 of IFT from the ciliary tips. These defects might stem from a reduction in the loading of IFT
485 components and dynein onto IFT trains at the ciliary base.
486
487

488

489 To better investigate the role of WDR-31, ELMD-1, and RPI-2 in IFT, we measured the
490 anterograde (middle and distal segment) and retrograde IFT velocities in wild type and triple
491 mutants. When compared to wild-type IFT speeds, we found a significant increase in the average
492 anterograde IFT velocities of IFT-74::GFP, IFT-140::GFP, OSM-3::GFP, and OSM-6::GFP in the
493 middle segments of triple mutant (**Fig. S7A, B, C, and D**), implying that the integrity of
494 anterograde IFT components is likely compromised. In contrast, in the triple mutant, the retrograde
495 and distal anterograde IFT velocities are unaltered. Taken together, our findings suggest that with
496 the exception of heterotrimeric Kinesin II, all IFT proteins studied, including dynein CHE-3,
497 OSM-3 kinesin, IFT-B, and IFT-A components, display certain defects in *wdr-31* related mutants,
498 either ciliary accumulations for dynein CHE-3, OSM-3 and IFT-B component or dim distal cilia
499 staining for IFT-A component and dynein motors (CHE-3 and XBX-1) or changes in IFT
500 velocities.

501

502 **WDR-31, ELMD-1, and RPI-2 restrict ciliary entry of non-ciliary proteins**

503 Given that WDR-31, ELMD-1, and RPI-2 localize at the base of cilia, we wanted to examine the
504 role of these proteins in the ciliary gate, and we chose the TRAM-1 protein (the ortholog of human
505 TRAM1), which surrounds the PCMC in *C. elegans* but stays outside of cilia (Williams et al.,
506 2011), as well as the transition fiber protein DYF-19 (human FBF1) and the transition zone
507 proteins NPHP-1 (the human NPHP1) and MKS-2 (human TMEM216) (Wei et al., 2013). We
508 showed that neither *wdr-31, elmd-1*, or *rpi-2* deletion, nor double mutant combinations, result in
509 ciliary entry of TRAM-1 or MKS-2 (**Fig. 7A and B)**, suggesting that neither of these alone affects
510 ciliary gating. In contrast, TRAM-1 protein leaks into cilia in all three independent *wdr-31* triple
511 mutants, but the majority of signal remains outside of cilia (**Fig. 7A and B**), whereas the

512 localizations of transition zone NPHP-1 and transition fiber protein DYF-19 remain unchanged
513 (**Fig. 7C**). In the *wdr-31;elmd-1;rpi-2* triple mutants, the PLC1-PH::GFP marker for
514 phosphatidylinositol 4,5-bisphosphate (PtdIns(4,5)P2) stays outside of cilia. In the wild type,
515 PLC1-PH::GFP stains PCMC membranes but does not penetrate cilia (**Fig. 7D)**. Furthermore, we
516 explored the localization of TAX-4, a ciliary membrane protein, and it remains unaffected in the
517 triple mutants (**Fig. 6SB**). Taken together, our findings reveal a functionally redundant role for
518 WDR31, ELMD-1, and RPI-2 in restricting entry of non-ciliary proteins into cilia, despite the fact
519 that TZ protein localization remains unchanged.
520
521 **WDR-31 and ELMD-1 are required for recruitment of BBS-7, a BBSome component, to cilia**
522 Some of IFT defects (cilia accumulations of IFT-B complex, weak cilia staining of IFT-A
523 components, and increased in IFT speed) observed in the *wdr-31;elmd-1;rpi-2* triple mutants are
524 reminiscent of IFT defects observed in several *bbs* mutants (Blacque, 2004; Ou et al., 2005; Wei
525 et al., 2012; Xu et al., 2015;). We hypothesized that the IFT complex destabilization defects in
526 triple mutants might be due to defects in the BBSome. First, we found that ciliary tip accumulations
527 of IFT-74:GFP, an IFT-B component, in *bbs-8(nx77)* mutants were comparably similar to that of
528 double and triple mutants (**Fig. 9A**). Furthermore, there is no further increase of IFT
529 accumulations in the triple mutants *wdr-31;elmd-1;bbs-8*.
530
531 We then investigated whether the ciliary localization of BBS-7::GFP, a core member of
532 the BBSome, is controlled by WDR-31, ELMD-1, and RPI-2, because the ciliary localization of
533 other BBSome components is dependent on other BBSome subunits (Ou et al., 2007). We predict
534 that the ciliary localization of BBSome is more likely disturbed in triple mutants, contributing to

535 the observed IFT abnormalities. Consistent with expectations, BBS-7::GFP is lost or significantly
536 diminished in the cilia of double and triple mutants, but BBS-7::GFP localization persists at the
537 ciliary base in these mutants (**Fig. 9B**). We next performed the time-lapse movie analysis of BBS-
538 7::GFP with kymography, which revealed that BBS-7::GFP movements were undetectable in 27%
539 and 42% of cilia in the head in double and triple mutants, respectively (**Supplementary Movie**
540 **S6)**. We were able to quantify the frequency of BBS-7::GFP even though the density of trajectories
541 (IFT particles) on kymographs was weak in double and triple mutants relative to wild type (**Fig.**
542 **9C**). Our analysis revealed a substantial decrease in the average of BBS-7::GFP particles
543 translocating in the anterograde and retrograde directions in the remaining worms that display IFT
544 (average anterograde and retrograde IFT particles: 0.55 n/s and 0.58 for wild type; 0.30 n/s and
545 0.33 n/s for double mutant; 0.07 n/s and 0.07 n/s for triple mutant, $p < 0.0001$; the Mann–Whitney
546 U test) (**Fig. 9C, D and Supplementary Movie S6**). We next used IFT-74::GFP to investigate IFT
547 speeds in *bbs-8* and its mutant combinations with *wdr-31* and *elmd-1*. The average velocities of
548 IFT-74::GFP in the middle segment of *bbs-8;wdr-31* and *bbs-8;wdr-31;elmd-1* were higher than
549 wild type, but were comparable to the *wdr-31;elmd-1;rpi-2* triple mutant (**Fig. S7A**). Taken
550 together, our results suggest that because the BBSome complex is unable to gain access to cilia in
551 double and triple mutants, IFT-B components and OSM-3/KIF17 likely accumulate excessively in
552 the distal portion of the cilia while IFT Complex A component staining the distal segment cilia
553 become dim (**Fig. 9E**).
554

555 **Discussion**

556 **WDR31 is a new ciliary protein encoding gene required for cilia biogenesis**

557 Clinical genomics, proteomics, functional genomics, and bioinformatics research have all
558 contributed to the expansion of the list of both ciliary and ciliopathy genes. Over 300 genes have
559 been identified as encoding ciliary proteins, including IFT-kinesin-dynein components, BSSome
560 components, structural ciliary components, signaling molecules, and IFT regulators, with many of
561 them being ciliopathy genes (Wheway et al., 2019; Vasquez et al., 2021). Our findings reveal the
562 roles of WDR-31, a member of the WD40-repeat protein (WDR) family, the ELMOD orthologue
563 (ELMD-1) and RP2 orthologue (retinitis pigmentosa 2; RPI-2) in cilia and IFT regulation. Several
564 members of the WD40-repeat protein family, including WDR34, WDR35, and WDR60, have
565 previously been connected to cilia, but the role of *WDR-31* in cilia has been unknown (Blacque et
566 al., 2006; Patel-King et al., 2013; Rompolas et al., 2007). Strikingly, we found that WDR31 is a
567 ciliary protein, and knocking it out in zebrafish using CRISPR/Cas9 causes ciliary defects,
568 including a decrease in the number of cilia in the LC. Furthermore, the link between WDR31 and
569 cilia was significantly strengthened by findings from *C. elegans*. First, the expression of the
570 *WDR31* orthologue (WDR-31) is restricted to the ciliated sensory neurons, and WDR-31 is
571 localized to ciliary compartments (the ciliary base and cilia) in C. elegans and human TERT-RPE1
572 cells. The exclusive cilia expression pattern of *wdr-31* in *C. elegans* is similar to that of ciliary and
573 ciliopathy genes like ARL-13/ALR13B, IFT, and BBS (Blacque et al., 2005). Second,
574 CRISPR/Cas9 mediated knock out of *WDR-31* combination with the ELMOD orthologue (ELMD-
575 1) and RP2 orthologue (retinitis pigmentosa 2; RPI-2) results in an abnormality in cilia functions
576 and structure in *C. elegans*. Our findings reveal that WDR31 is a new ciliary protein required for
577 cilia morphology in both zebrafish and *C. elegans*, suggesting the evolutionarily conserved role of
578 WDR31 in cilia biology.
579
580

581 **Functional redundancy between WDR-31, ELMD-1, and RPI-2**

582 Our genetic analysis in *C. elegans* provides evidence for functional redundancy for *wdr-31*, *elmd-*
583 *1*, and *rpi-2* in regulating cilia length, cilia morphology, and the trafficking of kinesin-IFT-
584 BBSome complexes. Though cilia length and cilia morphology are disrupted in *wdr-31;elmd-*
585 *1;rpi-2* triple mutants, with altered recruitment of kinesin, IFT, and BBS proteins and IFT
586 dynamics, simultaneous elimination of *elmd-1* and *rpi-2* did not result in severe defects in cilia
587 and IFT. Our interpretation for these data is that the additive defects in the triple mutants were
588 likely due to *wdr-31*, and WDR-31 is a central player in controlling cilia morphology and IFT
589 machinery. However, we cannot rule out the possibility of microtubule defects in cilia
590 ultrastructure in *elmd-1;rpi-2* double mutants. Additional work is needed, and a transmission
591 electron microscope (TEM) may be used to reveal further details in the ultrastructure of cilia in
592 these double mutants.

593

594 How do these proteins work together to regulate cilia-related phenotypes? While WDR31 is a
595 poorly characterized gene, the roles of human RP2 and ELMOD proteins in cilia biology are better
596 understood. Human RP2 localizes to the cilium and the basal body and displays GAP activity
597 toward two ARF family members, ARL2 and ARL3, both of which were linked to cilia biology
598 (Evans et al., 2010; Schwarz et al., 2017; Wright et al., 2011), while the ELMOD protein family
599 (ELMOD1-3) has GAP activity for ARL2 (ELMOD1 and ELMOD3) and ARF6 (ELMOD1)
600 (Ivanova et al., 2014; Jaworek et al., 2013; Johnson et al., 2012; Miryounesi et al., 2019).
601 ELMOD2 localizes to the basal body, and our study showed ELMOD3 localizes to cilium (Turn
602 et al., 2021). Taking into account the fact that RPI-2 and ELMD-1 are GAPs, and loss of these two
603 GAP proteins likely result in the overactivation of their target G proteins, how does WDR-31
604 function with these GAP proteins? One possibility is that WDR31 may function downstream of

605 regulatory GTPases, including ARL2, ARL3, or unidentified GTPases, activated by these GAP
606 proteins. One downside of this explanation is that *wdr-31* single mutants did not have significant
607 ciliary and IFT defects; but, if this were valid, we would expect to observe further anomalies in
608 cilia and IFT in *wdr-31* single mutants, close to the removal of these three genes. Alternatively,
609 the activity/function of overactive GTPases can be somehow regulated by WDR-31, maybe WDR-
610 31 may have a GAP activity for the regulatory GTPases or it may have a GTPase activity. While
611 WDR-31 does not seem to have a GAP domain, HHMER search revealed that human WDR31 has
612 a distant sequence resemblance to a nucleoside-triphosphatase (NTPase) domain (NACHT)
613 containing protein in *Penicillium camemberti* (Gabler et al., 2020). PSI-BLAST search confirmed
614 this result (unpublished data).
615
616 Furthermore, the ciliary roles of these two GAP proteins might be independent of their GAP
617 activities, and consistent with this idea, the recent study showed the ciliary roles of ELMOD2 are
618 partially independent of its GAP activity (Turn et al., 2021). However, a variety of evidence
619 suggests that WDR31 and ELMOD3 do not form a complex. First, mass spectrometry-based
620 proteomic analysis for either WDR31 or ELMOD3 showed that neither WDR31 nor ELMOD3
621 contains each other or RP2 (unpublished data). Second, the proper localization of any of these
622 three proteins was independent of each other (unpublished data). Further studies are needed to
623 understand a mechanistic link between WDR31, ELMOD, and RP2, and figure out the independent
624 contributions of WDR31 and both GAP proteins in cilia biology.
625
626 **A potential function for WDR31-ELMOD-RP2 in determining the integrity of ciliary gate**
627 Our findings that worm lacking WDR31-ELMOD-RP2 also display ciliary entrance of non-ciliary
628 proteins (TRAM-1) suggests that these proteins may play a function in the ciliary gate. Despite the

629 mechanism by which these proteins regulate the ciliary gate functions remains unknown, the
630 abnormality of IFT proteins (abnormal distribution and increased anterograde IFT velocities) in
631 triple mutant may provide some hint about the potential roles of these proteins in ciliary gate. One
632 possible explanation is that the IFT defect in triple mutant potentially results in compromised
633 ciliary gate function. Consistent with this possibility, it was previously reported that in *C. elegans,*
634 the elimination of IFT complex A components and cytoplasmic dynein motor CHE-3 result in a
635 defect in ciliary gate function (Jensen et al., 2018; Scheidel and Blacque, 2018).
636

637 **The WDR31-ELMOD-RP2 is needed for efficient IFT entry and IFT dynamics**

638 Our findings show that simultaneous disruption of *WDR-31*, *ELMD-1*, and *RPI-2* causes
639 differential effects on ciliary IFT protein localizations, including accumulation of IFT-B
640 subcomplex components (IFT-74 and OSM-6), dynein (CHE-3) and kinesin motor (OSM-3) or
641 dim cilia staining of IFT-A subcomplex component and a dynein component (CHE-11 and XBX-
642 1) or almost no cilia entry of a BBSome component (BBS-7). Furthermore, with the exception of
643 cytoplasmic dynein CHE-3, the triple mutant shows a significant decrease in moving IFT particles
644 along cilia in both directions for almost all IFT proteins, indicating that the combined elimination
645 of WDR-31, ELMD-1, and RPI-2 has a significant impact on ciliary recruitment of IFT/BBSome
646 components (IFT-74, OSM-6, CHE-11, and BBS-7) and OSM-3. Our *in vivo* time lapse movie
647 analysis indicated that anterograde IFT velocities for OSM-3, OSM-6, IFT-74, and CHE-11 in the
648 middle segment of cilia are considerably increased in the triple mutant, while IFT velocities in the
649 distal segment of cilia and retrograde direction are unaltered (**Fig. 8A, B, C and D**). This suggests
650 that in cilia lacking *WDR-31, ELMD-1*, or *RPI-2*, certain portions of these IFT proteins are not
651 effectively loaded onto anterograde IFT.

652 Based on our results, which involve increase in anterograde IFT speed, a decrease in
653 moving IFT particles in anterograde and retrograde transport, ciliary tip aggregation of OSM-
654 3/KIF17 and IFT-B, and failure of docking of BBSome to the IFT machinery, we propose that
655 some of these defects likely stem from the failure of BBSome to associate with moving IFT in
656 cilia in double and triple mutants. These proteins are likely regulator for IFT/BBSome. Consistent
657 with our proposal, the almost comparable IFT/BBSome phenotypes were reported with
658 hypomorphic mutations in *dyf-2* (WDR19 orthologue, an IFT-A component) and *bbs-1* (a BBSome
659 component), where they showed that while BBSome remains at the base of cilia and does not
660 undergo IFT, the failure of IFT-B reassociation with IFT-A at the ciliary tips results in IFT-B
661 ciliary tip accumulations, despite the fact the association of IFT-A and IFT-B components in
662 anterograde transport persists (Wei et al., 2012). They proposed that the BBSome controls the IFT
663 assembly at the ciliary base and IFT turnover at the ciliary tip. However, several of the
664 abnormalities identified in the triple mutant, such as diminished IFT frequencies and ectopic
665 projection from the ciliary base, are unlikely to be related to BBSome dysfunction in the triple
666 mutant, because our findings revealed that the IFT frequency in the *bbs-8* mutant stays intact. Plus,
667 we did not observe ectopic project from the ciliary base in the *bbs-8* mutant (Data not shown).
668
669 However, the IFT defects in the triple mutant are unlikely to be due to mislocalization of
670 transition fiber proteins such as DYF-19 (the FBF1 orthologue), which was implicated in
671 regulating the ciliary entry of IFT and BBSome, since our data showed that the localization of
672 DYF-19 was not impaired in the triple mutants (Wei et al., 2013).
673 On the other hand, the effect on IFT might be direct since RP2 was previously proposed to
674 control the intraflagellar transport protein IFT20 pool in the peri-basal body and trafficking of
675 Kif17 and Kif7 to the ciliary tip (Schwarz et al., 2017). However, several interesting questions

676 have yet to be resolved: what is the mechanism by which WDR-31-ELMD-1-RPI-2 regulates the
677 ciliary entry of the BBSome entry? How does WDR-31-ELMD-1-RPI-2 interact with proteins,
678 including ARL6, that regulate the BBSome recruitment (Jin et al., 2010)? Future study research
679 will help us to understand how these proteins regulate BBSome/IFT trafficking. In summary, this
680 study provides a mechanistic explanation of the function of WDR-31, a new ciliary protein,
681 ELMD-1, and RPI-2 in the regulation of cilia biogenesis and also contributes a new regulator for
682 IFT/BBSome.
683

684 **Acknowledgments**

685 We thank Oliver Blacque, Piali Sengupta, Micheal Leroux, the National BioResource Project
686 (NBRP) in Japan, and the CGC in the United States, which is financed by the NIH Office of
687 Research Infrastructure Programs (P40 OD010440) for sharing valuable strains. We thank Oliver
688 Blacque and Samuel Katz for critical reading of the manuscript. We thank the Abdullah Gul
689 University Scientific Research Project Coordination Unit (Project number: TOA-2018-110) for
690 providing the funding that initiated the project. M.U. was supported by the Tistou & Charlotte
691 Kerstan Stiftung. The Leica laser scanning microscope was funded by a grant from Deutsche
692 Forschungsgemeinschaft (INST 2388/62-1).
693
694
695
696
697

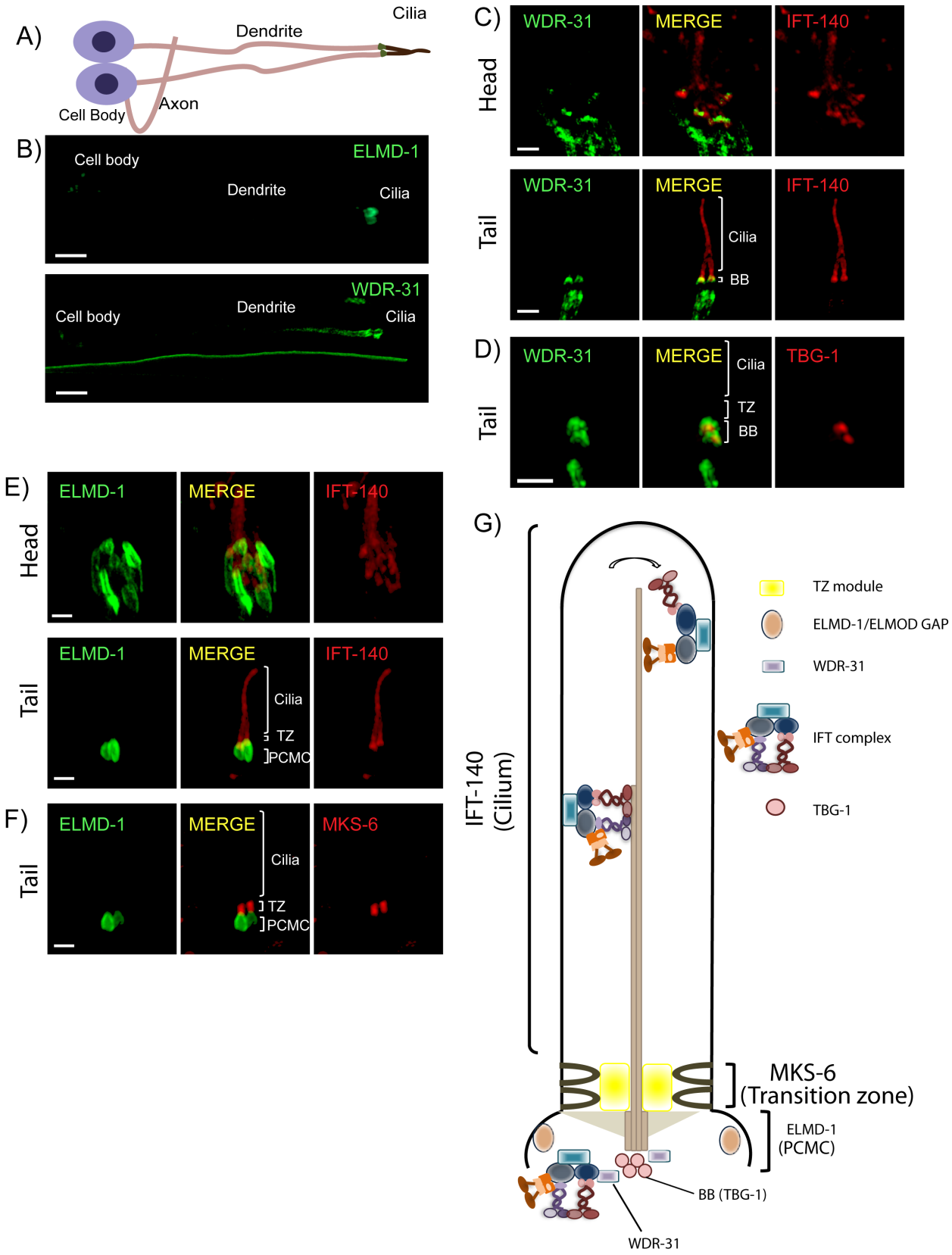
A)
Cilia
Dendrite
Axon
Cell Body
B)
Cell body
ELMD-1
Dendrite
Cilia
WDR-31
Cell body
Dendrite
Cilia
C)
Head
WDR-31
MERGE
IFT-140
Tail
WDR-31
MERGE
IFT-140
Cilia
BB
D)
Tail
WDR-31
MERGE
Cilia
TZ
BB
TBG-1
E)
Head
ELMD-1
MERGE
IFT-140
Tail
ELMD-1
MERGE
IFT-140
Cilia
TZ
PCMC
F)
Tail
ELMD-1
MERGE
MKS-6
Cilia
TZ
PCMC
G)
IFT-140
(Cilium)
TZ module
ELMD-1/ELMOD GAP
WDR-31
IFT complex
TBG-1
MKS-6
(Transition zone)
ELMD-1
(PCMC)
BB (TBG-1)
WDR-31

698

699 **Figure 1: WDR-31/WDR31 and ELMD-1/ELMOD proteins are evolutionary conserved**
700 **ciliary proteins A, B)** Shown are the representative drawing of the PHA/PHB sensory neuron
701 (phasmid neurons located in the tail). Cilia, dendrite, axon and cell soma (cell body) are depicted
702 in the drawing. Fluorescence images from the transgenic strain carrying WDR-31::GFP or
703 GFP::ELMD-1 were displayed in the PHA/PHB sensory neurons. Scale bars: 3 μm **C, D)** Co-
704 localization of WDR-31::GFP (Green) with the IFT-140::mCherry (Red, an IFT-A component, a
705 ciliary marker) or TBG-1:mKate (Red, γ-Tubulin, the basal body) in the tail (phasmids) and head
706 (amphid) sensory neurons. TZ and BB denote the transition zone and the basal body, respectively
707 **E, F)** GFP::ELMD-1 (Green) localizes to the BB and PCMC (the periciliary membrane
708 compartment) proximal to the transition zone. Co-labelling of GFP::ELMD-1 with MKS-
709 6:mCherry marker (transition zone) or IFT-140::mCherry in the tail (phasmids) and head (amphid)
710 neurons. Scale bars: 2 μm **G)** Shown are representative localizations of WDR-31 and ELMD-1.
711

A)

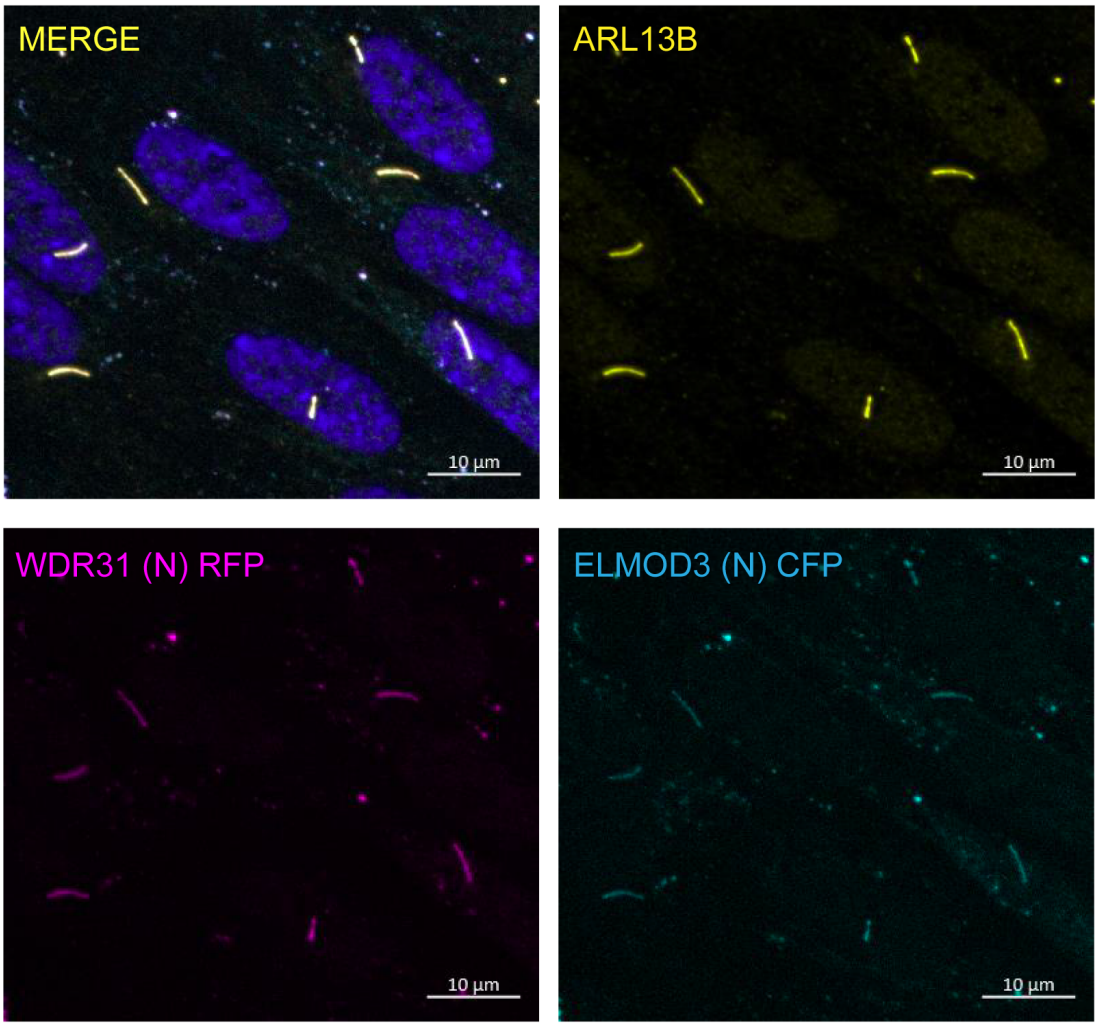
MERGE
10 µm
ARL13B
10 µm
WDR31 (N) RFP
10 µm
ELMOD3 (N) CFP
10 µm

B)

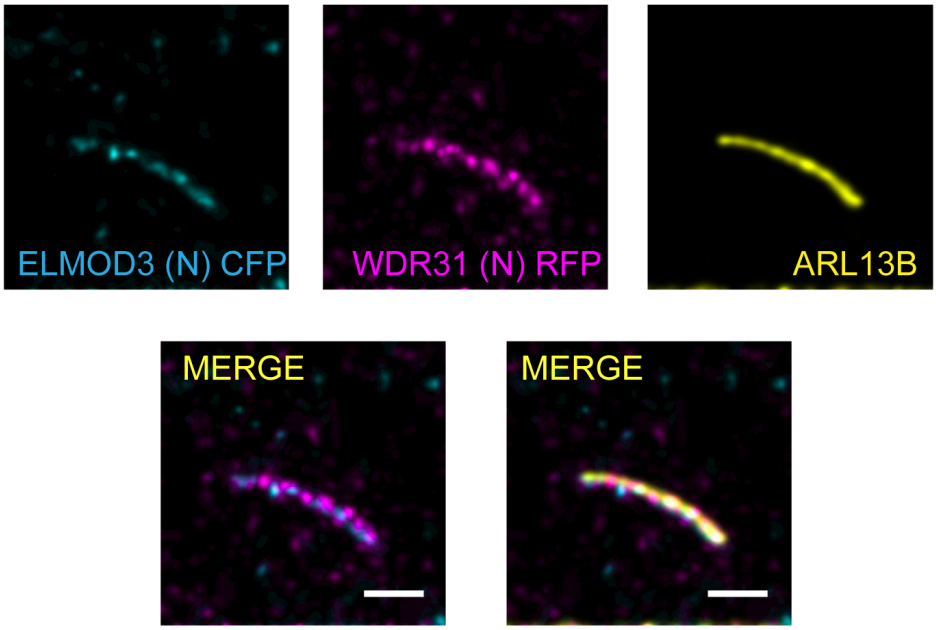
ELMOD3 (N) CFP
WDR31 (N) RFP
ARL13B
MERGE
MERGE

712

713 **Figure 2**: **ELMOD3 and WDR31 localize to the primary cilium**. **A, B**) Shown are the staining
714 of WDR31 (tagged with cyan fluorescent protein) and ELMOD3 (tagged with red fluorescent
715 protein) together with a ciliary marker ARL13B and DAPI (nucleus) in hTERT-RPE1 cells.
716 hTERT-RPE1 cells were transiently transfected with 100 ng of WDR31:CFP and ELMOD3:RFP.
717 Scale bars: 10 µm (A) and 3 µm (B)
718

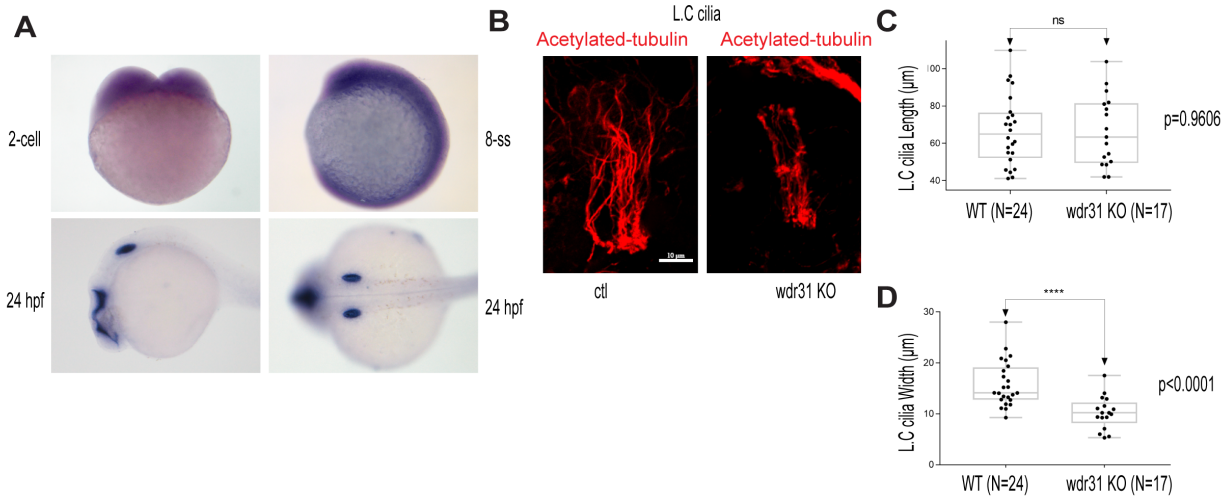

719

720 **Figure 3: WDR31 regulates ciliogenesis in zebrafish A)** Shown are the expression pattern
721 analysis of WDR31 in zebrafish embryos. *Wdr31* is ubiquitously expressed before the
722 segmentation stage (2 cell and 8 somite stages (SS). The expression of *Wdr31* becomes limited to
723 the otic vesicle and brain region at 24 hours post fertilization (24 hpf). **B)** Shown are cilia of lateral
724 crista (LC) of the otic vesicle, stained with acetylated-tubulin, in wild type and *Wdr31* knockout,
725 generated via CRISPR/Cas9. **C and D**) The length of cilia in the lateral crista (LC) of the otic
726 vesicle remains unaffected in zebrafish *Wdr31* knockout while the cilia number is decreased, as
727 shown with the measurement of width of cilia lateral crista (LC) of the otic vesicle.
728
729

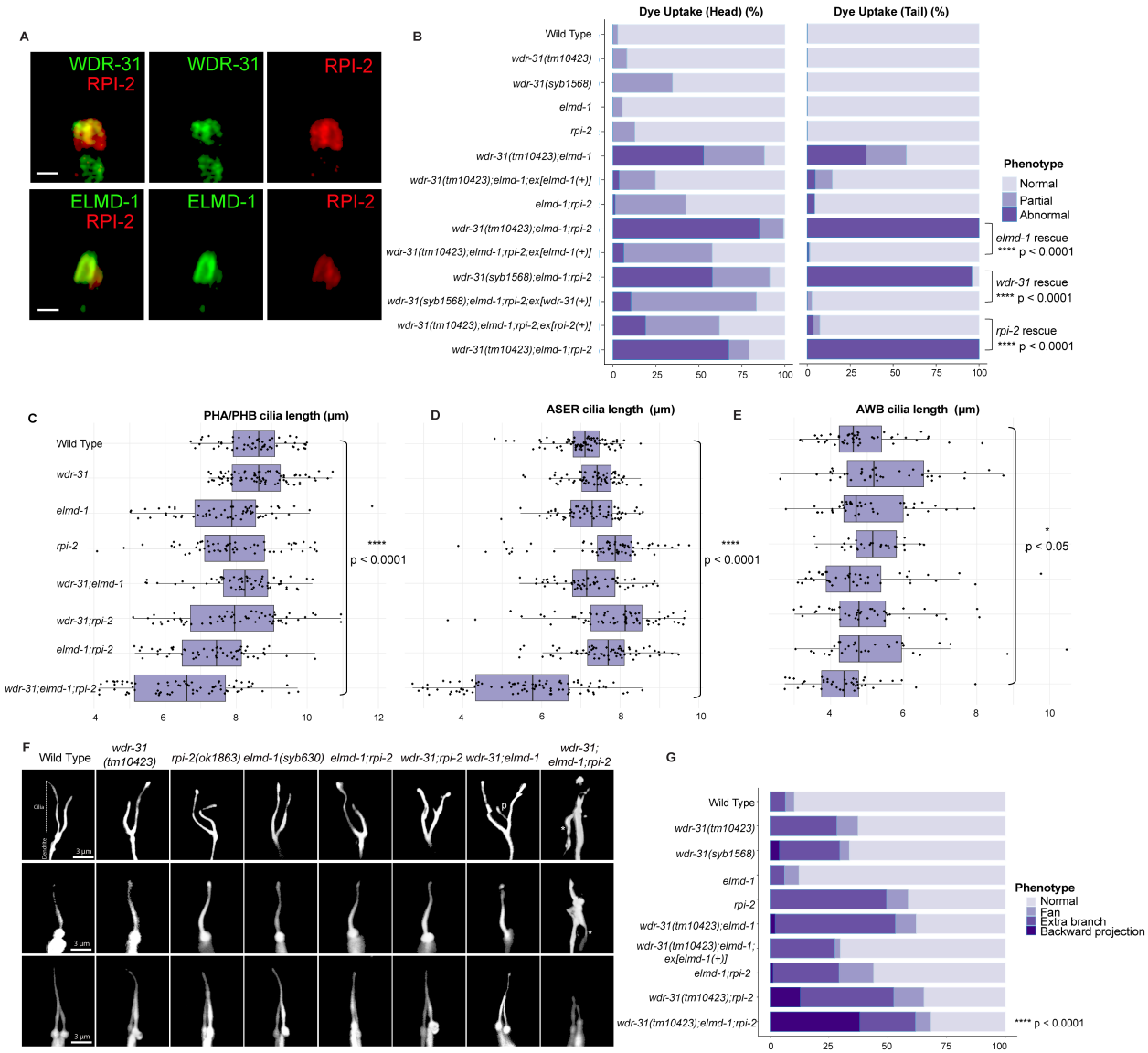

Figure 4: WDR31-ELMOD-RP2 are needed for determining cilia length and morphology in *C. elegans*

A) Shown are co-localizations of RPI-2::mCherry (red, the endogenously labeled RPI-2) with either WDR-31::GFP (green, the endogenously labeled WDR-31) or GFP::ELMD-1 (green, overexpressed) in tail (phasmid) sensory neurons in *C. elegans.* Scale bars: 1 µm. **B)** The fraction of the dye uptake defects is presented in bar charts for wild type and the indicated mutants. Fisher's exact test was performed for statistical analysis between indicated triple mutants and a rescue gene

738 for Dye assay. Brackets show statistical significance between two strains compared ($p < 0.0001$
739 and **** indicate statistical significance). **C, D, E)** Shown is the jitter plot for PHA/PHB cilia,
740 ASER cilia and AWB short cilia length (μm) for wild type and indicated mutant strains. Statistical
741 significance between wild type and triple mutants was shown with bracket. **** implies statistical
742 significance which means that p value is lower than $p < 0.0001$ while * means that p value is lower
743 than $p < 0.05$. **F)** Fluorescence images show the morphology of AWB cilia (fork-like structure
744 located in the head), ASER cilia (amphid channel cilia) and PHA/PHB cilia (phasmid channel
745 cilia) in wild type and indicated mutant backgrounds. The backward projection from the cilia is
746 shown with asterisks (*) while p indicates the ectopic projections from the middle parts of cilia.
747 Scale bars: 3 μm **G)** The percentage of the abnormality in AWB cilia morphology is depicted in
748 bar charts. Fisher's exact test was utilized for statistical analysis of AWB cilia morphology between
749 wild type and designated mutants, and **** denotes statistical significance.
750

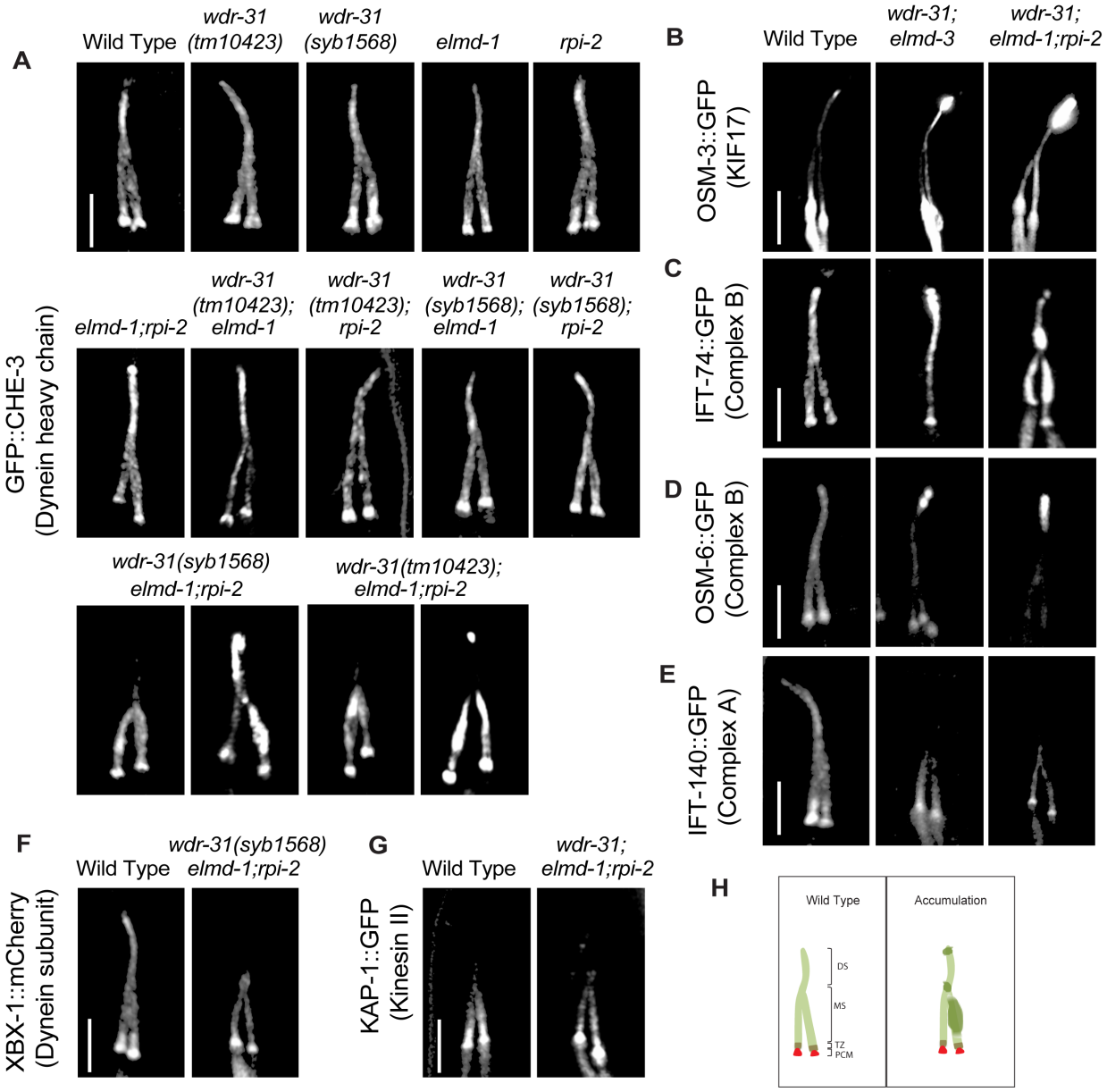

Figure 5: IFT-B proteins and OSM-3/KIF17 accumulate at the ciliary tip. Shown are fluorescent images of PHA/PHB cilia (phasmid tail). **A)** Fluorescent images from a single copy GFP::CHE-3 (human dynein heavy chain DYNC2H1) in wild type and indicated mutant backgrounds are displayed. GFP::CHE-3 accumulations within cilia and dim distal cilia staining

756 were observed in two distinct triple mutants (*wdr-31(tm10423);elmd-1;rpi-2* and *wdr-*
757 *31(syb1568);elmd-1;rpi-2).* Scale bars: 3 µm **B, C, D, E, F)** Confocal microscopy analysis of IFT-
758 A (IFT-140::GFP) and IFT-B complex components (OSM-6/IFT52::GFP and IFT-74::GFP)
759 revealed differential abnormalities in the transport of IFT-A and IFT-B components in double
760 (w*dr-31;elmd-1*) and triple mutants. The localization of XBX-1::mCherry (Dynein subunit) in
761 *wdr-31(syb1568);elmd-1;rpi-2* triple mutants phenocopies the dim distal cilia staining of IFT-A
762 (IFT-140::GFP) in the w*dr-31(tm10423);elmd-1;rpi-2* triple mutants. OSM-3/KIF17 Kinesin
763 motor accumulates at the ciliary tips in w*dr-31(tm10423);elmd-1* double and w*dr-*
764 *31(tm10423);elmd-1;rpi-2* triple mutants. Compared to double mutants, the ciliary tip staining is
765 stronger in the triple mutants. Scale bars: 3 µm **G)** Fluorescent images from Kinesin II motor
766 (KAP-1::GFP) revealed that the restricted middle segment localization of KAP-1 remains
767 unchanged in w*dr-31(tm10423);elmd-1;rpi-2* triple mutants. Scale bars: 3 µm **H)** Shown are the
768 drawings of phasmid cilia (PHA/PHB sensory neurons in the tail) in wild type and mutants
769 showing ciliary accumulations.
770
771
772
773
774
775
776
777
778

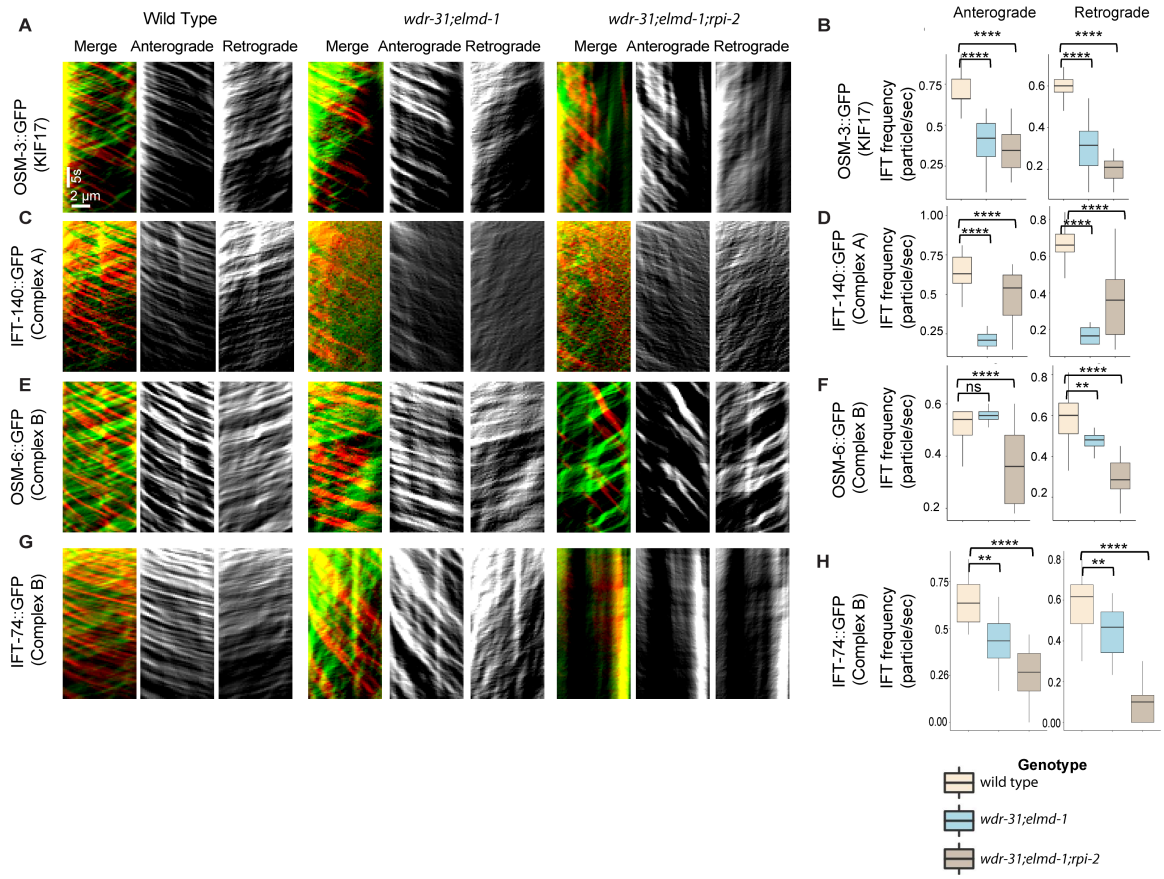

Figure 6: Measurement of anterograde and retrograde IFT transport frequency A, C, E and G) Shown are representative kymographs of GFP tagged IFT proteins translocating in the tail cilia (PHA/PHB sensory neurons) of wild type and indicated mutants. Kymographs for anterograde, retrogrades and merged (Red & Green) were generated with ImageJ equipped with KymographClear. The trajectory represents a moving IFT particle, and the average number of moving IFT particles in wild type and indicated mutants (double, triple) was calculated by counting all trajectories in each kymograph. Travel time and distance are shown on kymographs. **B, D, F and H)** Box-and-Whisker charts with error bars were created to visualize the average number of IFT anterograde and retrograde particles between wild type and indicated mutants. The Mann–Whitney U test was used to measure statistical analysis and significance. The four and three

asterisks (**** and ***) at the top of the brackets indicate that the p value between the two strains is less than 0.0001 and 0.001, respectively, suggesting statistical significance. Ns stands for "not significant."

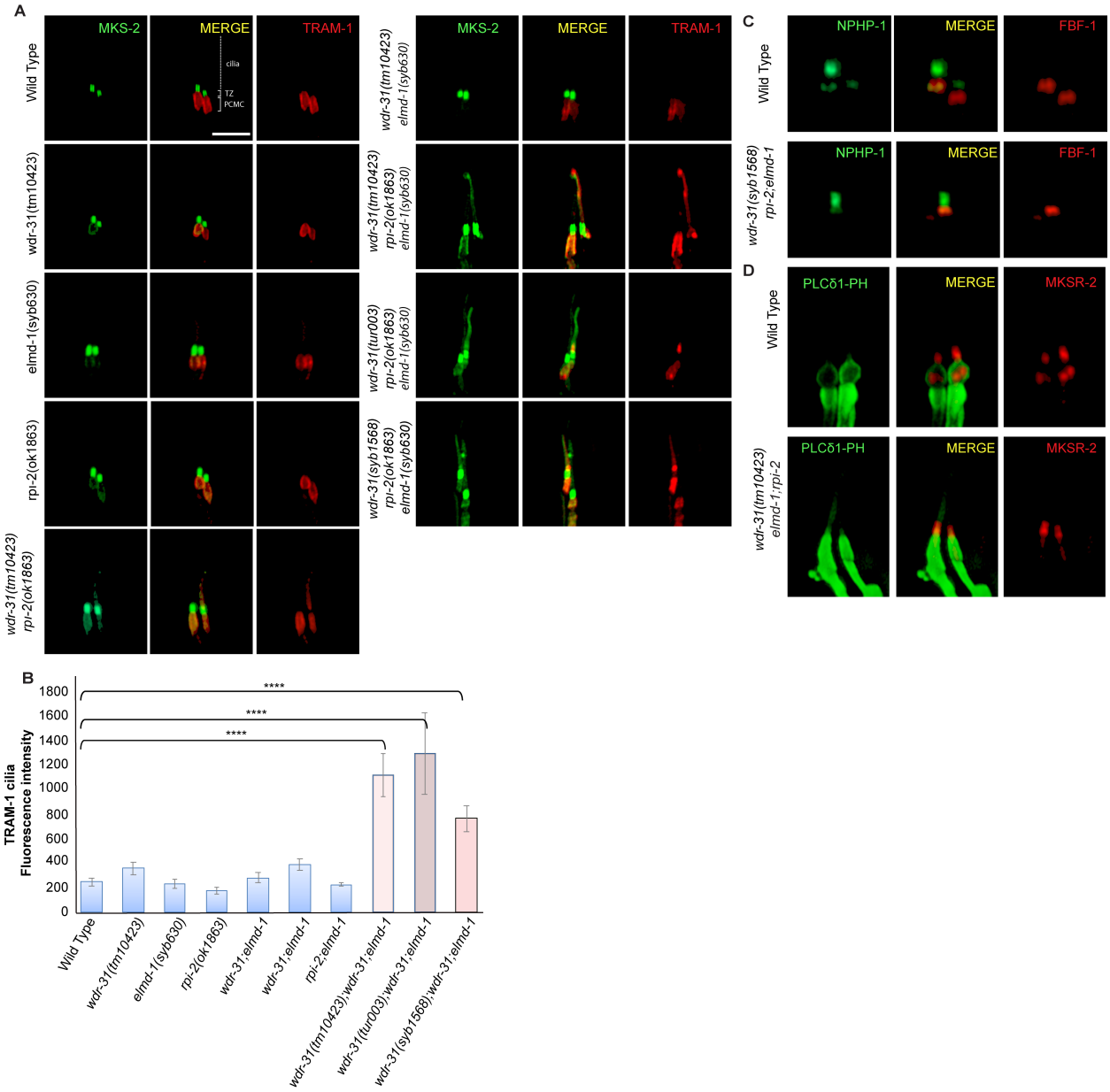

Figure 7: A non-ciliary membrane protein TRAM-1 enters into cilia in *wdr-31;elmd-1;rpi-2* triple mutants. A) Confocal fluorescent images exhibit the localization of tdTomato tagged

798 TRAM-1 (a PCMC marker) and MSK-2::GFP (a TZ marker) in wild type and indicated mutants.
799 TRAM-1 leaks into cilia in all three *wdr-31* triple mutants. Cilia, the periciliary membrane
800 compartment (PCMC), and transition zone (TZ) are depicted in the fluorescent image. Scale bars:
801 2 μm, **B)** TRAM-1 fluorescence intensities in cilia were measured in wild type and designated
802 mutants, and the results were shown in the plot. The four asterisks (****) indicate statistically
803 significant differences between the wild type and the identified triple mutants. **C)** The localization
804 of NPHP-1::GFP (a transition zone protein) and FBF-1::mCherry (a transition fiber protein) was
805 similar unaffected in *wdr-31;elmd-1;rpi-2* triple mutants **D)** The PLCδ1-PH::GFP (a marker for
806 monitoring phosphatidylinositol 4,5-bisphosphate (PtdIns(4,5)P2) in the plasma membrane)
807 decorates the membranes of PCMC and does not enter into cilia in wild type. MKSR-2 was used
808 to mark the transition zone. The PLCδ1-PH::GFP stays outside of cilia in the *wdr-31;elmd-1;rpi-*
809 *2* triple mutants.
810
811

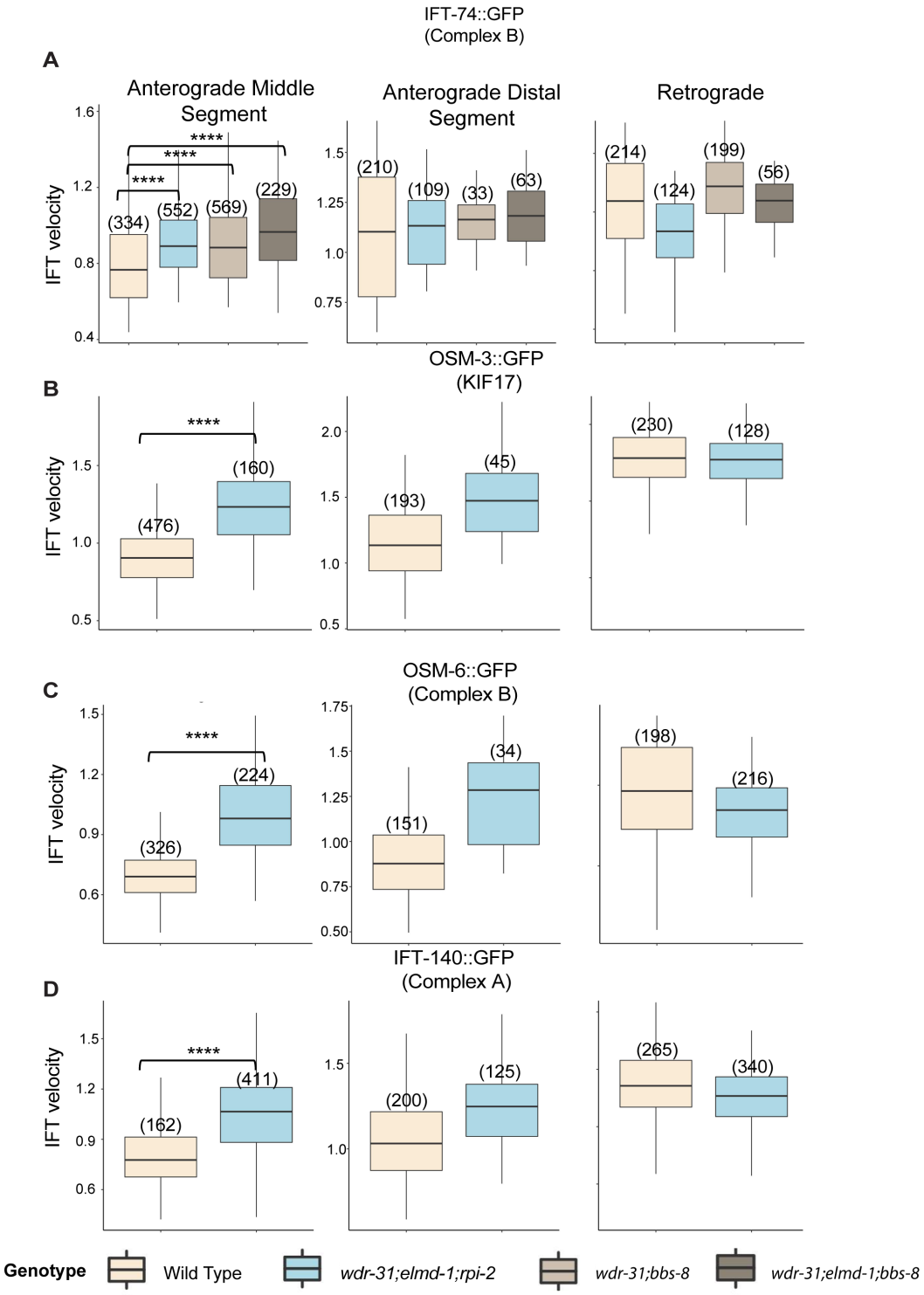
IFT-74::GFP
(Complex B)
A
Anterograde Middle Segment
Anterograde Distal Segment
Retrograde
IFT velocity
****
(334)
(552)
(569)
(229)
(210)
(109)
(33)
(63)
(214)
(124)
(199)
(56)
OSM-3::GFP
(KIF17)
B
(476)
(160)
(193)
(45)
(230)
(128)
OSM-6::GFP
(Complex B)
C
(326)
(224)
(151)
(34)
(198)
(216)
IFT-140::GFP
(Complex A)
D
(162)
(411)
(200)
(125)
(265)
(340)
Genotype
Wild Type
wdr-31;elmd-1;rpi-2
wdr-31;bbs-8
wdr-31;elmd-1;bbs-8

812

813 **Figure 8: The average anterograde IFT velocities were significantly increased in *wdr-*
814 ***13;elmd-1;rpi-2* triple mutants, A, B, C, and D)** The average anterograde (distal and middle
815 segments) and retrograde IFT velocities were calculated, and box-and-whisker plots with error
816 bars were used to depict them. Numbers shown at the top of bars represent the number of IFT
817 particles used for determining IFT velocities. To compare statistical analysis and significance
818 between wild type and specified mutations, the Mann–Whitney U test was performed. A p value
819 of less than 0.0001 indicates statistical significance between the two strains, as shown by the four
820 asterisks (****) at the top of the brackets.
821

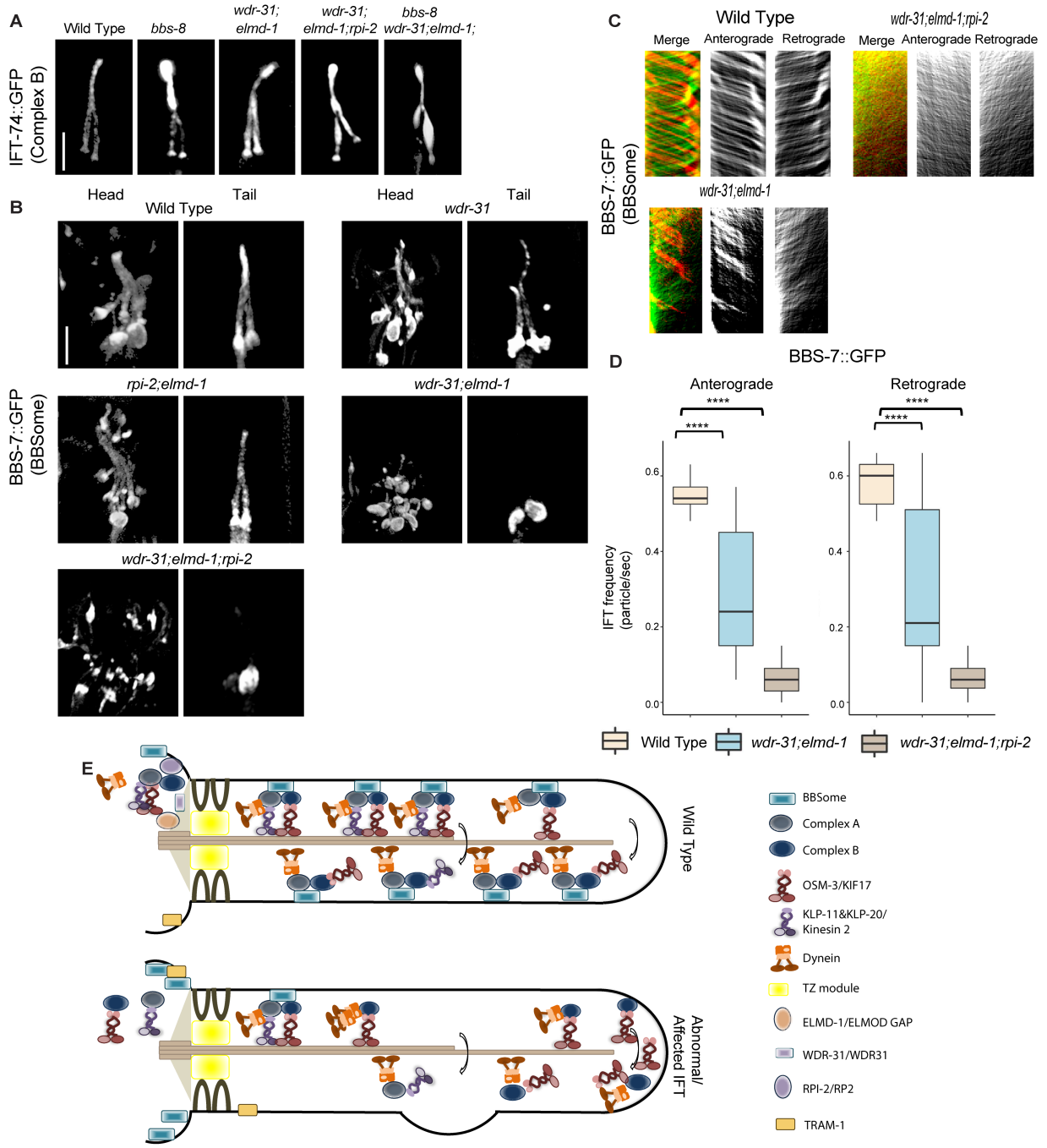

822

823 **Figure 9: WDR-31 and ELMD-1 regulate the recruitment of BBSome to cilia.**

824 **A)** Shown are fluorescence images from the transgenic strain carrying IFT-74::GFP, an IFT-B

825 component, in wild type, *wdr-31;elmd-1* double mutants, *wdr-31;elmd-1;rpi-2* and *wdr-31;elmd-*

826 *1;bbs-8* triple mutants, and *bbs-8(nx77)*. The IFT-B subunit IFT-74:GFP accumulates at the ciliary

827 tips and cilia in the tail of all three mutants. **B)** Confocal fluorescence images showing the
828 localization of BBS-7:GFP, a BBSome subunit, in the heads and tails of wild type and *wdr-*
829 *31(tm10423); wdr-31;elmd-1*; *rpi-2;elmd-1* double and *wdr-31;elmd-1;rpi-2* triple mutants.
830 Fluorescence images showed absent or weak cilia staining of BBS-7::GFP in both the head and
831 tails of *wdr-31;elmd-1* and *wdr-31;elmd-1;rpi-2* triple mutants. **C)** Kymographs were created from
832 time-lapse BBS-7::GFP movies (PHA/PHB cilia) using KymographClear integrated into ImageJ.
833 Shown are representative kymographs for BBS-7::GFP translocating in wild type and indicated
834 mutants. Each trajectory in kymographs was counted. Travel time and distance are included on
835 kymograph **D)** The graph depicts the average number of BBS-7::GFP particles traveling around
836 cilia in both directions for wild type and indicated mutants. The Mann–Whitney U test revealed
837 statistical significance between the compared strains and that the p value was less than 0.0001
838 shown by the four asterisks (****) at the top of the brackets **E)** In wild type, the assembly of the
839 Kinesin-IFT-BBSome complex (Kinesin-II and OSM-3**,** IFT-B , IFT-A and BBSome) happens at
840 the base of cilia. In the middle segment of amphid and phasmid cilia in *C. elegans*, both
841 heterotrimeric Kinesin II and homodimeric OSM-3 transport the IFT-A- IFT-B- BBSome complex
842 in an anterograde direction. Heterotrimeric Kinesin II returns to the ciliary base when it reaches
843 the tip of the middle segment of amphid and phasmid cilia, whereas homodimeric OSM-3 is
844 responsible for the anterograde translocation of the IFT-BBSome complex in the distal segment of
845 amphid and phasmid cilia. When the OSM-3-IFT-BBSome complex reaches the ciliary tip,
846 cytoplasmic dynein transports them back to the ciliary base. In *wdr-31;elmd-1* double *wdr-*
847 *31;elmd-1;rpi-2* triple mutants, the BBSome failed to enter into cilia, thus leading to accumulations
848 of OSM-3 and IFT-B components in the ciliary tips.
849

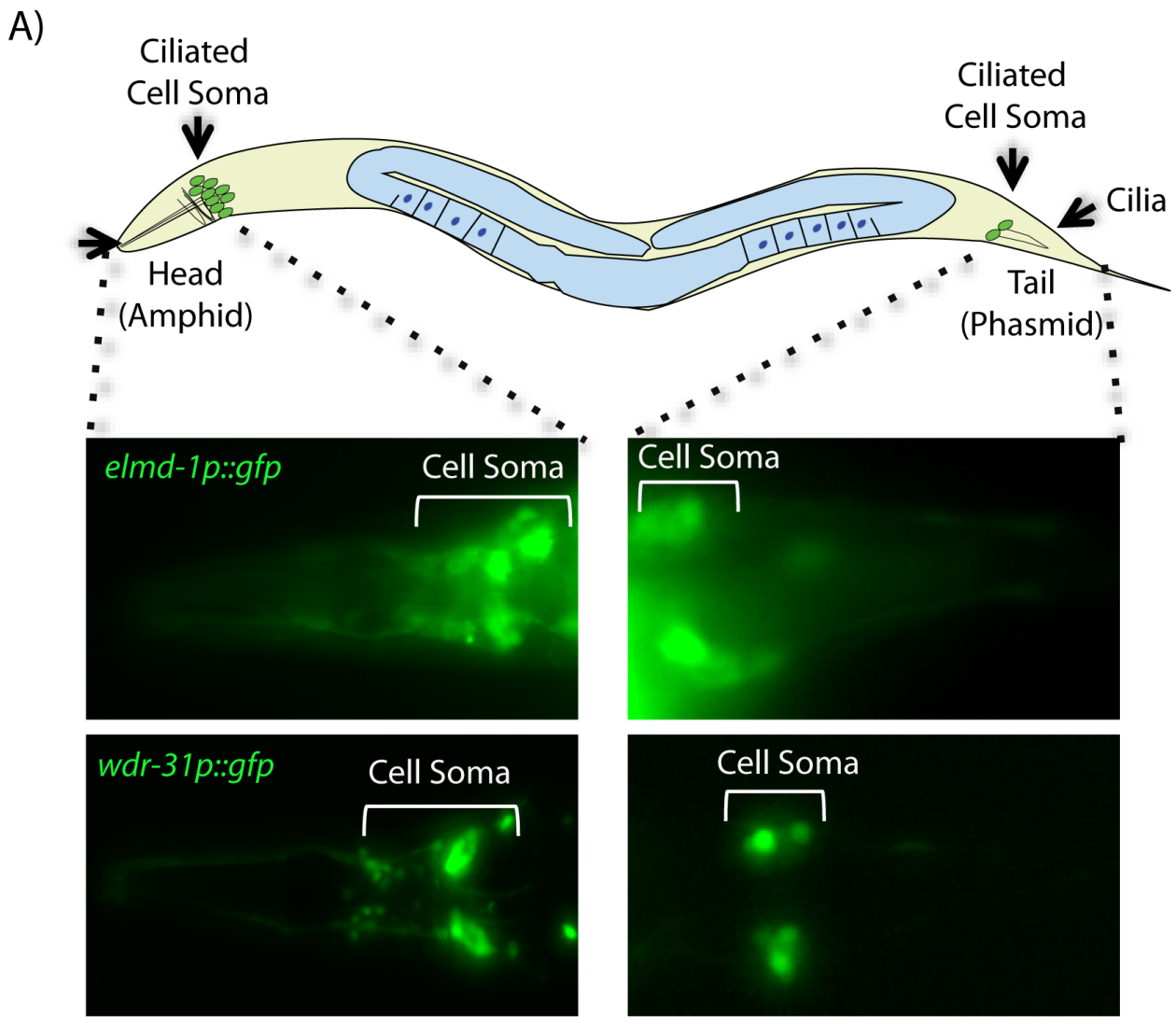

Supplementary Figure 1: Expression patterns of WDR-31 and ELMD-1. A) A total of 60 sensory neurons are distributed in the head (amphid) and tails (phasmid) of *C. elegans.* The ciliated sensory neurons are displayed in the schematic of *C. elegans.* The expression of *elmd-1promoter::gfp* (1000 kb) and *wdr-31promoter::gfp* (1000 kb) were shown in the fluorescence images. The cell of ciliated sensory neurons (cell soma) in the head and tails were displayed in brackets.

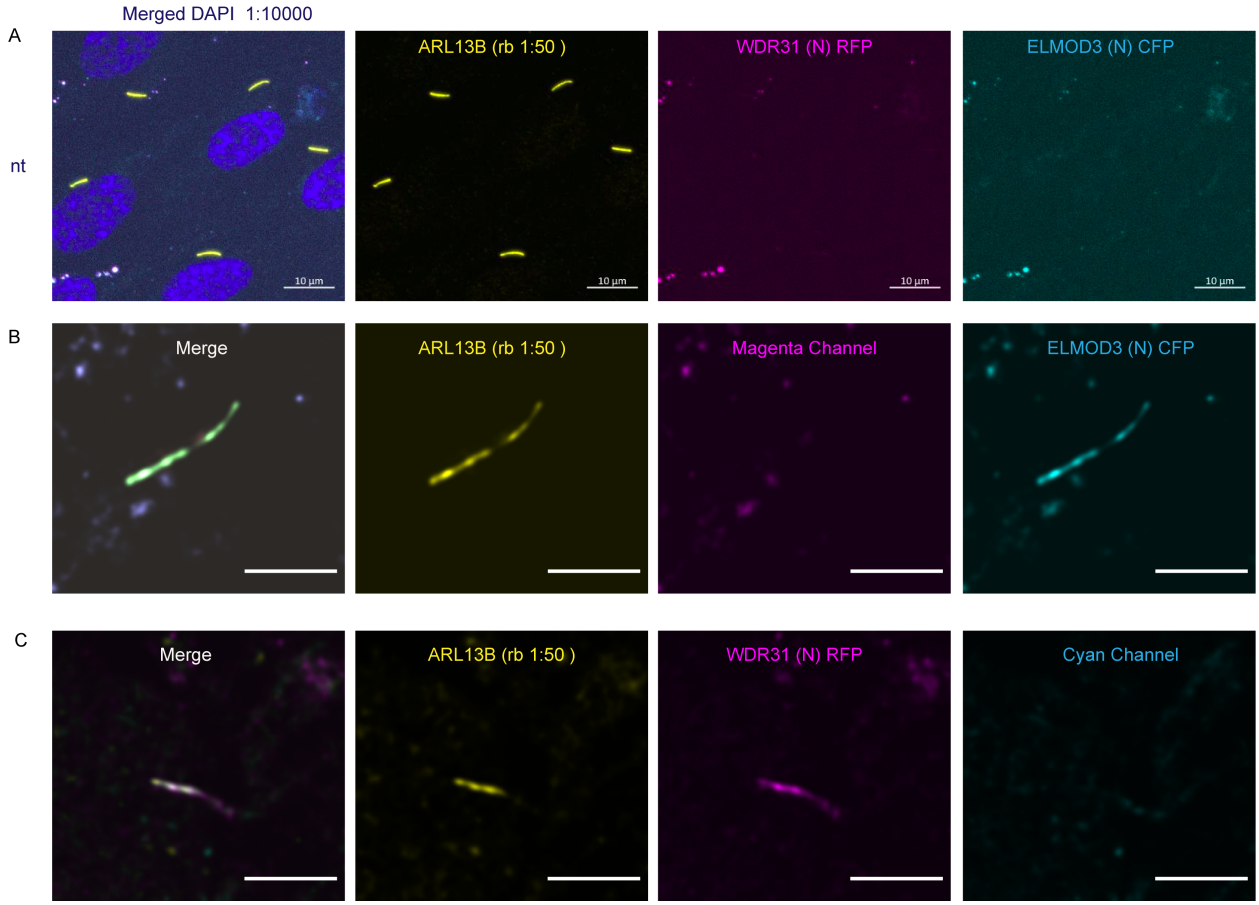

Supplementary Figure 2: Ciliary localization of WDR31 and ELMOD3 in hTERT-RPE1 cells A) Images showing immunostaining of a ciliary marker ARL13B and DAPI (nucleus) in hTERT-RPE1 cells. NT represents no transfection of hTERT-RPE1 with WDR31 (tagged with cyan fluorescent protein) and ELMOD3 (tagged with red fluorescent protein). Scale bars: 10 µm. **B)** Images showing immunostaining of hTERT-RPE1 cells transfected with ELMOD3-CFP (cyan) and also stained for ARL13B (yellow). The magenta channel only shows some background but no localization to the cilium. Green regions in the "merge" picture show co-localization of both ELMOD3 and ARL13B proteins. Scale bars: 3 µm. **C)** Fluorescence images displaying hTERT-RPE1 Fluorescence images of immunostaining for ARL13B (yellow) and WDR31-RFP (magenta) in hTERT-RPE1 cells transfected with WDR31-RFP (cyan). The cyan channel shows some

870 background, with no cilium localisation. WDR31 and ARL1B proteins are co-localized in the pink

871 sections of the "merge" image. Scale bars: 3 µm.

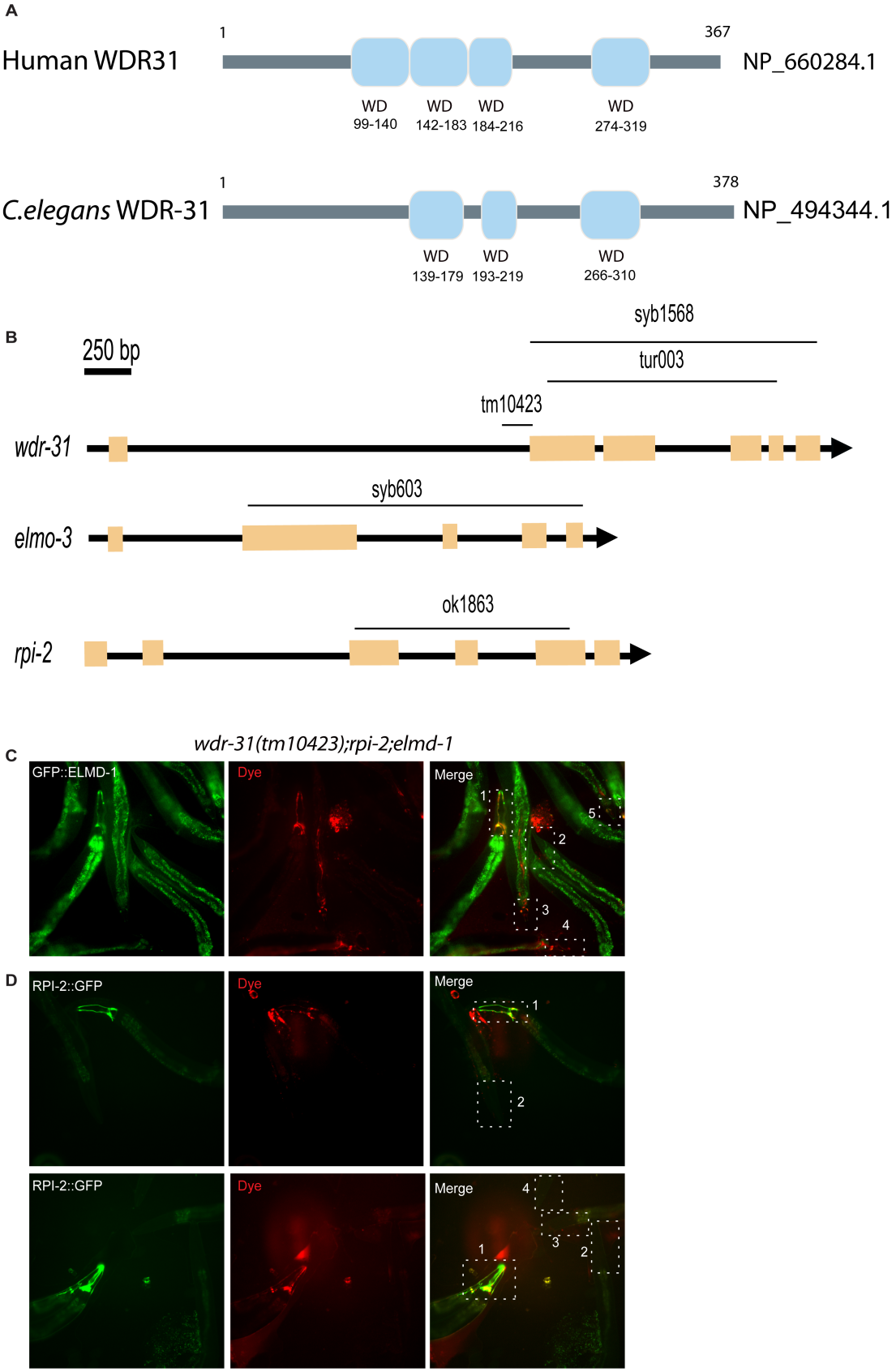
A
Human WDR31
1
367
NP_660284.1
WD 99-140
WD 142-183
WD 184-216
WD 274-319
C.elegans WDR-31
1
378
NP_494344.1
WD 139-179
WD 193-219
WD 266-310
B
250 bp
syb1568
tur003
tm10423
wdr-31
syb603
elmo-3
ok1863
rpi-2
C
wdr-31(tm10423);rpi-2;elmd-1
GFP::ELMD-1
Dye
Merge
D
RPI-2::GFP
Dye
Merge
RPI-2::GFP
Dye
Merge

872

873 **Supplementary Figure 3: Rescue of dye uptake defects by ELMD-1 or RPI-2.**

874 **A)** Shown are representative schematics of human and *C. elegans* WDR-31/WDR31. Human
875 WDR31 (NP_660284.1) has four WD domains while *C. elegans* WDR-31 (NP_494344.1) has
876 three WD domains (https://prosite.expasy.org/; Sigrist CJA et al 2012). **B)** Schematic diagrams of
877 *wdr-31*, *elmd-1* and *rpi-2* together with corresponding deletions are shown. Scale bars: 250 bp. **C**
878 **and D**) Fluorescence microscope images of mutant worms (head and tail) with red-fluorescent dye
879 uptake (texas red filter) and GFP-tagged ELMD-1 and RPI-2 (fluorescence filter set for GFP) are
880 shown. The head or tail in the dotted lines is indicated by numbers in the combined fluorescence
881 images. GFP expression in combination with RED fluorescence indicates the rescue of dye uptake
882 defects.

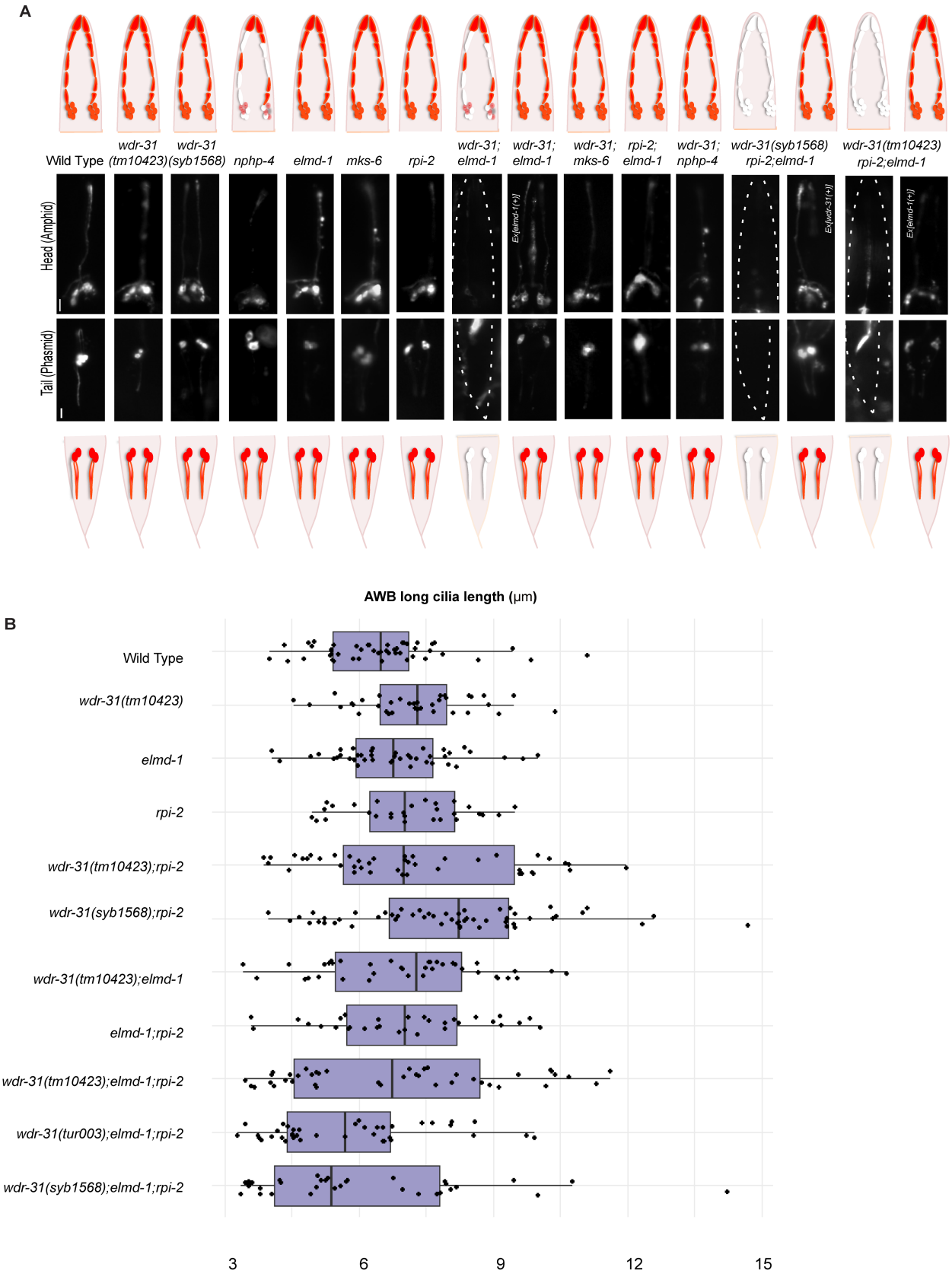
A
Wild Type
wdr-31 (tm10423)
wdr-31 (syb1568)
nphp-4
elmd-1
mks-6
rpi-2
wdr-31; elmd-1
wdr-31; elmd-1
wdr-31; mks-6
rpi-2; elmd-1
wdr-31; nphp-4
wdr-31(syb1568) rpi-2;elmd-1
wdr-31(tm10423) rpi-2;elmd-1
Ex[elmd-1(+)]
Ex[wdr-31(+)]
Ex[elmd-1(+)]
Head (Amphid)
Tail (Phasmid)
B
AWB long cilia length (µm)
Wild Type
wdr-31(tm10423)
elmd-1
rpi-2
wdr-31(tm10423);rpi-2
wdr-31(syb1568);rpi-2
wdr-31(tm10423);elmd-1
elmd-1;rpi-2
wdr-31(tm10423);elmd-1;rpi-2
wdr-31(tur003);elmd-1;rpi-2
wdr-31(syb1568);elmd-1;rpi-2
3
6
9
12
15

883

884 **Supplementary Figure 4: AWB cilia morphology in WDR-31-ELMD-1-RPI-2 triple mutants**
885 **A)** Shown are the schematic representations of lipophilic fluorescent dye uptake in the head
886 (amphid) and tail (phasmid) sensory neurons in *C. elegans.* Red labelling indicates the normal dye
887 uptake while the failure of Dye uptake was shown in white. Fluorescence images show the dye
888 update in the head and tail neurons in the wild type and indicated mutant strains. No dye uptake
889 was observed in both head (amphid) and tail (phasmid) of *wdr-31(tm10423);elmd-1* double
890 mutants, *wdr-31(tm10423);elmd-1;rpi-2* and *wdr-31(syb1568);elmd-1;rpi-2* triple mutants.
891 *Ex[elmd-1(+)*] rescues the dye uptake defects of *wdr-31(tm10423);elmd-1* double and *wdr-*
892 *31(tm10423);elmd-1;rpi-2* triple mutants, while *Ex[wdr-31(+)]* rescues the Dye uptake defects of
893 *wdr-31(syb1568);elmd-1;rpi-2* triple mutants. Scale bars: 10 µm. **B)** Shown is the jitter plot for
894 AWB long cilia length (µm) in wild type and mutant strains.

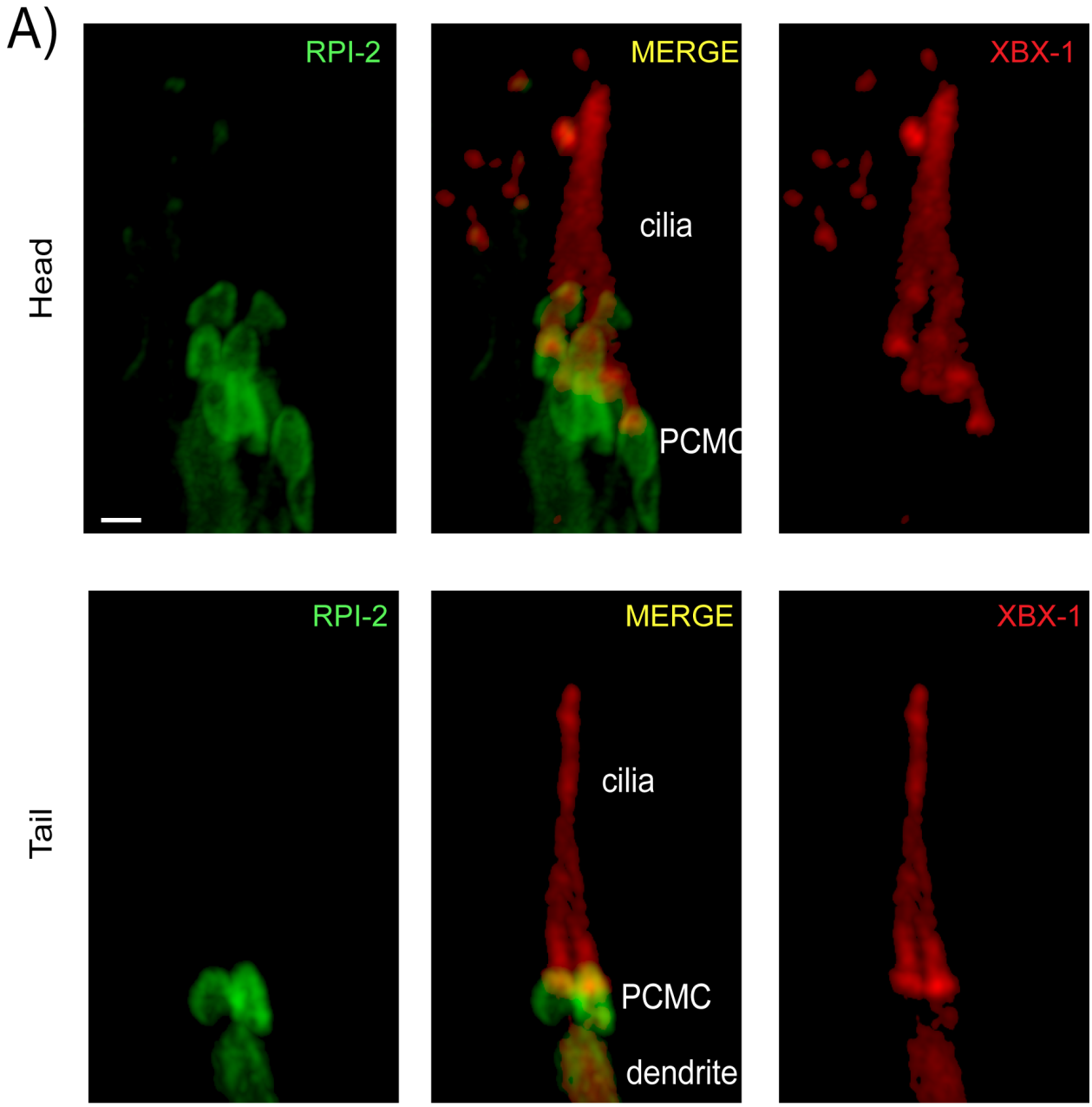

895

896 **Supplementary Figure 5: A)** Shown is co-localization of RPI-2::GFP (human RP2) and XBX-
897 1::mCherry (human DYNC2LI1) in the head and tail sensory neurons. XBX-1 stains the entire
898 cilium and is used as a ciliary marker while RPI-2 is located at PCMC. PCMC denotes the
899 periciliary membrane compartment.

900

901

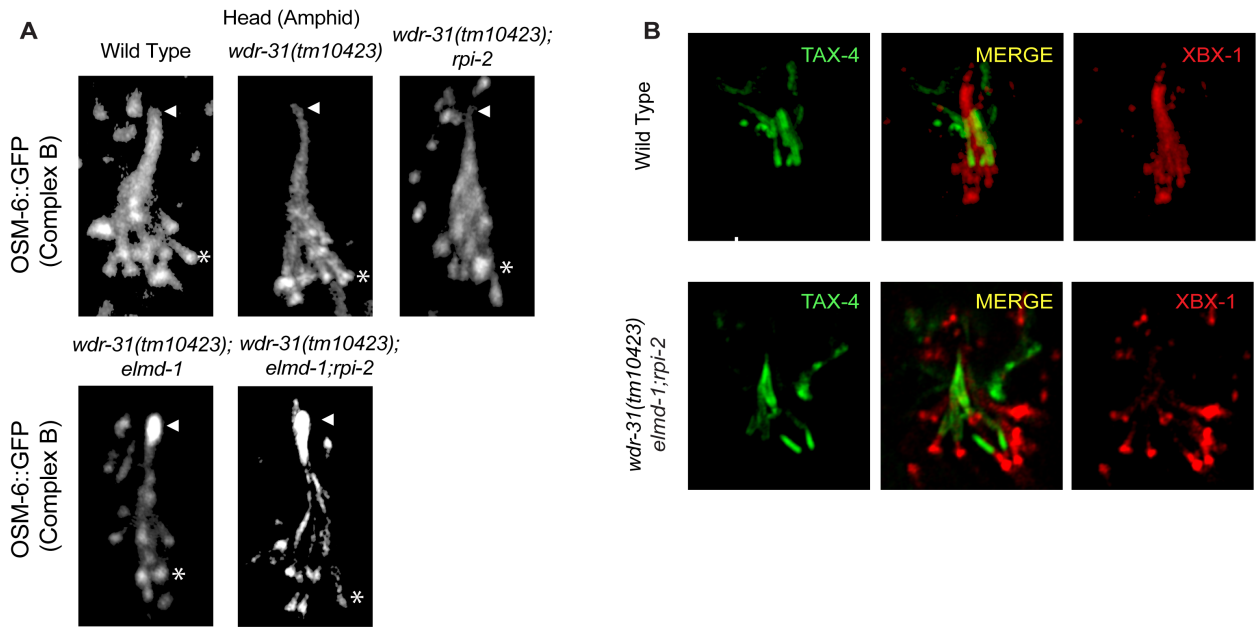

Supplementary Figure 6: A) Confocal images (Z-stack) display the localization of OSM-6::GFP (a single copy transgene, huma IFT52) in the head (a bunch of cilia) of wild type and indicated mutants. Arrow points the ciliary tips while asterisks indicate the ciliary base. **B)** Confocal images show colocalization of TAX-4 (a ciliary membrane protein) and XBX-1::tdTomato (a cilia marker).

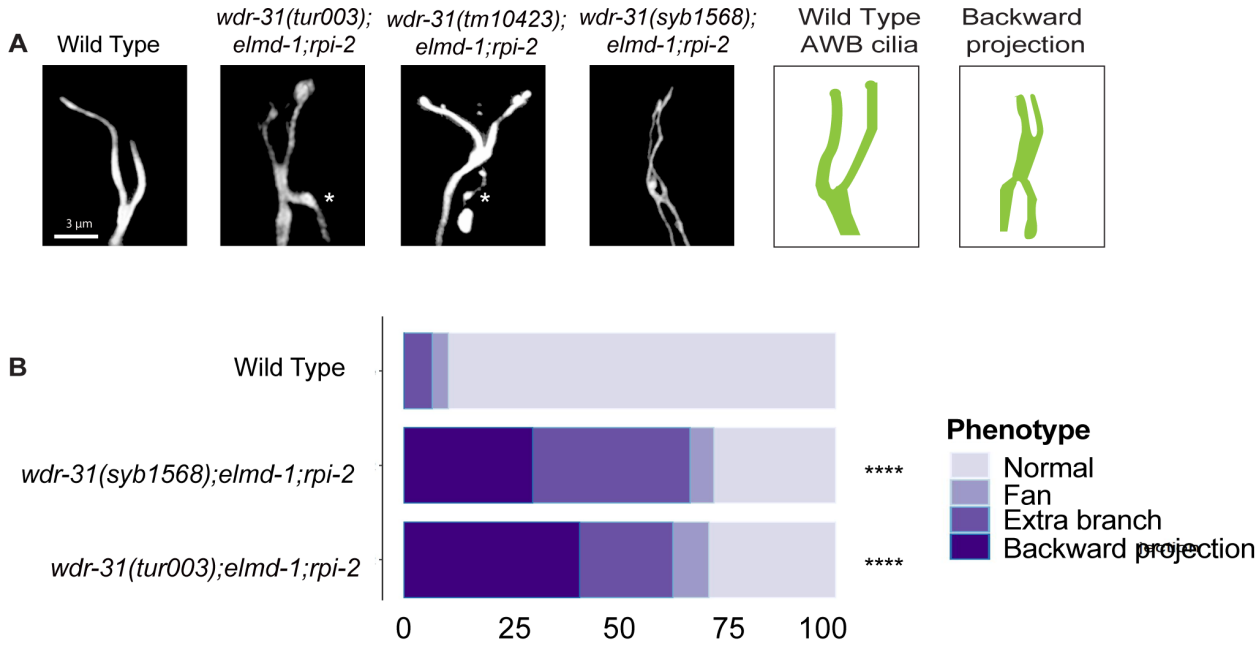

909 **Supplementary Figure 7: A)** The architecture of AWB cilia (a fork-like structure in the head) in
910 wild type and mutant backgrounds is shown in fluorescent images. In schematic illustrations, the
911 AWB cilia in wild type and altered mutants are illustrated. **B)** Shown are bar plots displaying
912 percentage of phenotypes in wild type and indicated triple mutants. Four asterisks (****) indicates
913 statistical significances between wild type and indicated triple mutants.

914 **Supplementary Movies**

915 For the IFT assay, time-lapse movies (3 frames per second) were generated with Leica DM6, and
916 were processed with Image J to generate GIFs (10 fps).

917 **Supplementary Movies:**

918 **Supplementary Movie 1:** IFT-74::GFP in wild type and indicated mutant backgrounds.

919 **Supplementary Movie 2:** OSM-6::GFP in wild type and indicated mutant backgrounds.

920 **Supplementary Movie 3:** OSM-3::GFP in wild type and indicated mutant backgrounds

921 **Supplementary Movie 4:** GFP::CHE-3 in wild type and indicated mutant backgrounds.

922 **Supplementary Movie 5:** IFT-140::GFP in wild type and indicated mutant backgrounds.

923 **Supplementary Movie 6:** BBS-7::GFP in wild type and indicated mutant backgrounds.

924 **References**

925 Ansley, S.J., Badano, J.L., Blacque, O.E., Hill, J., Hoskins, B.E., Leitch, C.C., Chul Kim, J.,
926 Ross, A.J., Eichers, E.R., Teslovich, T.M., Mah, A.K., Johnsen, R.C., Cavender, J.C.,
927 Alan Lewis, R., Leroux, M.R., Beales, P.L., Katsanis, N., 2003. Basal body dysfunction
928 is a likely cause of pleiotropic Bardet–Biedl syndrome. Nature 425, 628–633.
929 https://doi.org/10.1038/nature02030
930
931 Anvarian, Z., Mykytyn, K., Mukhopadhyay, S., Pedersen, L.B., Christensen, S.T., 2019. Cellular
932 signalling by primary cilia in development, organ function and disease. Nat. Rev.
933 Nephrol. 15, 199–219. https://doi.org/10.1038/s41581-019-0116-9
934
935 Arnaiz, O., Malinowska, A., Klotz, C., Sperling, L., Dadlez, M., Koll, F., Cohen, J., 2009. Cildb:
936 a knowledgebase for centrosomes and cilia. Database 2009.
937 https://doi.org/10.1093/database/bap022
938

939 Avidor-Reiss, T., Maer, A.M., Koundakjian, E., Polyanovsky, A., Keil, T., Subramaniam, S.,
940 Zuker, C.S., 2004. Decoding Cilia Function. Cell 117, 527–539.
941 https://doi.org/10.1016/S0092-8674(04)00412-X
942
943 Blacque, O., E., 2008. Intraflagellar transport: from molecular characterisation to mechanism.
944 Front. Biosci. 13, 2633. https://doi.org/10.2741/2871
945
946 Blacque, O.E., 2004. Loss of C. elegans BBS-7 and BBS-8 protein function results in cilia
947 defects and compromised intraflagellar transport. Genes Dev. 18, 1630–1642.
948 https://doi.org/10.1101/gad.1194004
949
950 Blacque, O.E., Li, C., Inglis, P.N., Esmail, M.A., Ou, G., Mah, A.K., Baillie, D.L., Scholey,
951 J.M., Leroux, M.R., 2006. The WD Repeat-containing Protein IFTA-1 Is Required for
952 Retrograde Intraflagellar Transport. Mol. Biol. Cell 17, 5053–5062.
953 https://doi.org/10.1091/mbc.e06-06-0571
954
955 Blacque, O.E., Perens, E.A., Boroevich, K.A., Inglis, P.N., Li, C., Warner, A., Khattra, J., Holt,
956 R.A., Ou, G., Mah, A.K., McKay, S.J., Huang, P., Swoboda, P., Jones, S.J.M., Marra,
957 M.A., Baillie, D.L., Moerman, D.G., Shaham, S., Leroux, M.R., 2005. Functional
958 Genomics of the Cilium, a Sensory Organelle. Curr. Biol. 15, 935–941.
959 https://doi.org/10.1016/j.cub.2005.04.059
960
961 Blacque, O.E., Sanders, A.A., 2014. Compartments within a compartment: What *C. elegans* can
962 tell us about ciliary subdomain composition, biogenesis, function, and disease.
963 Organogenesis 10, 126–137. https://doi.org/10.4161/org.28830
964
965 Bloodgood, R.A., 2009. From Central to Rudimentary to Primary: The History of an
966 Underappreciated Organelle Whose Time Has Come.The Primary Cilium, in: Methods in
967 Cell Biology. Elsevier, pp. 2–52. https://doi.org/10.1016/S0091-679X(08)94001-2
968
969 Brenner, S., 1974. The genetics of Caenorhabditis elegans. Genetics 77, 71–94.
970
971 Breslow, D.K., Hoogendoorn, S., Kopp, A.R., Morgens, D.W., Vu, B.K., Kennedy, M.C., Han,
972 K., Li, A., Hess, G.T., Bassik, M.C., Chen, J.K., Nachury, M.V., 2018. A CRISPR-based
973 screen for Hedgehog signaling provides insights into ciliary function and ciliopathies.
974 Nat. Genet. 50, 460–471. https://doi.org/10.1038/s41588-018-0054-7
975
976 Chang, N., Sun, C., Gao, L., Zhu, D., Xu, X., Zhu, X., Xiong, J.-W., Xi, J.J., 2013. Genome
977 editing with RNA-guided Cas9 nuclease in Zebrafish embryos. Cell Res. 23, 465–472.
978 https://doi.org/10.1038/cr.2013.45
979
980 Choksi, S.P., Babu, D., Lau, D., Yu, X., Roy, S., 2014. Systematic discovery of novel ciliary
981 genes through functional genomics in the zebrafish. Development 141, 3410–3419.
982 https://doi.org/10.1242/dev.108209
983
984 Dickinson, D.J., Ward, J.D., Reiner, D.J., Goldstein, B., 2013. Engineering the Caenorhabditis

985 elegans genome using Cas9-triggered homologous recombination. Nat. Methods 10,
986 1028–1034. https://doi.org/10.1038/nmeth.2641
987
988 Evans, R.J., Schwarz, N., Nagel-Wolfrum, K., Wolfrum, U., Hardcastle, A.J., Cheetham, M.E.,
989 2010. The retinitis pigmentosa protein RP2 links pericentriolar vesicle transport between
990 the Golgi and the primary cilium. Hum. Mol. Genet. 19, 1358–1367.
991 https://doi.org/10.1093/hmg/ddq012
992
993 Gabler, F., Nam, S., Till, S., Mirdita, M., Steinegger, M., Söding, J., Lupas, A.N., Alva, V.,
994 2020. Protein Sequence Analysis Using the MPI Bioinformatics Toolkit. Curr. Protoc.
995 Bioinforma. 72. https://doi.org/10.1002/cpbi.108
996
997
998 Herman, R.K., Hedgecock, E.M., 1990. Limitation of the size of the vulval primordium of
999 Caenorhabditis elegans by lin-15 expression in surrounding hypodermis. Nature 348,
1000 169–171. https://doi.org/10.1038/348169a0
1001
1002 Ivanova, A.A., East, M.P., Yi, S.L., Kahn, R.A., 2014. Characterization of Recombinant
1003 ELMOD (Cell Engulfment and Motility Domain) Proteins as GTPase-activating Proteins
1004 (GAPs) for ARF Family GTPases. J. Biol. Chem. 289, 11111–11121.
1005 https://doi.org/10.1074/jbc.M114.548529
1006
1007 Jaworek, T.J., Richard, E.M., Ivanova, A.A., Giese, A.P.J., Choo, D.I., Khan, S.N., Riazuddin,
1008 Sheikh, Kahn, R.A., Riazuddin, Saima, 2013. An Alteration in ELMOD3, an Arl2
1009 GTPase-Activating Protein, Is Associated with Hearing Impairment in Humans. PLoS
1010 Genet. 9, e1003774. https://doi.org/10.1371/journal.pgen.1003774
1011
1012 Jensen, V.L., Carter, S., Sanders, A.A.W.M., Li, C., Kennedy, J., Timbers, T.A., Cai, J.,
1013 Scheidel, N., Kennedy, B.N., Morin, R.D., Leroux, M.R., Blacque, O.E., 2016. Whole-
1014 Organism Developmental Expression Profiling Identifies RAB-28 as a Novel Ciliary
1015 GTPase Associated with the BBSome and Intraflagellar Transport. PLOS Genet. 12,
1016 e1006469. https://doi.org/10.1371/journal.pgen.1006469
1017
1018 Jensen, V.L., Lambacher, N.J., Li, C., Mohan, S., Williams, C.L., Inglis, P.N., Yoder, B.K.,
1019 Blacque, O.E., Leroux, M.R., 2018. Role for intraflagellar transport in building a
1020 functional transition zone. EMBO Rep. 19. https://doi.org/10.15252/embr.201845862
1021
1022 Jin, H., White, S.R., Shida, T., Schulz, S., Aguiar, M., Gygi, S.P., Bazan, J.F., Nachury, M.V.,
1023 2010. The Conserved Bardet-Biedl Syndrome Proteins Assemble a Coat that Traffics
1024 Membrane Proteins to Cilia. Cell 141, 1208–1219.
1025 https://doi.org/10.1016/j.cell.2010.05.015
1026
1027 Johnson, K.R., Longo-Guess, C.M., Gagnon, L.H., 2012. Mutations of the Mouse ELMO
1028 Domain Containing 1 Gene (Elmod1) Link Small GTPase Signaling to Actin
1029 Cytoskeleton Dynamics in Hair Cell Stereocilia. PLoS ONE 7, e36074.
1030 https://doi.org/10.1371/journal.pone.0036074

1031
1032
1033 Kaplan, O.I., Doroquez, D.B., Cevik, S., Bowie, R.V., Clarke, L., Sanders, A.A.W.M., Kida, K.,
1034 Rappoport, J.Z., Sengupta, P., Blacque, O.E., 2012. Endocytosis Genes Facilitate Protein
1035 and Membrane Transport in C. elegans Sensory Cilia. Curr. Biol. 22, 451–460.
1036 https://doi.org/10.1016/j.cub.2012.01.060
1037
1038 Lambacher, N.J., Bruel, A.-L., van Dam, T.J.P., Szymańska, K., Slaats, G.G., Kuhns, S.,
1039 McManus, G.J., Kennedy, J.E., Gaff, K., Wu, K.M., van der Lee, R., Burglen, L.,
1040 Doummar, D., Rivière, J.-B., Faivre, L., Attié-Bitach, T., Saunier, S., Curd, A., Peckham,
1041 M., Giles, R.H., Johnson, C.A., Huynen, M.A., Thauvin-Robinet, C., Blacque, O.E.,
1042 2016. TMEM107 recruits ciliopathy proteins to subdomains of the ciliary transition zone
1043 and causes Joubert syndrome. Nat. Cell Biol. 18, 122–131.
1044 https://doi.org/10.1038/ncb3273
1045
1046 Lechtreck, K.-F., Johnson, E.C., Sakai, T., Cochran, D., Ballif, B.A., Rush, J., Pazour, G.J.,
1047 Ikebe, M., Witman, G.B., 2009. The Chlamydomonas reinhardtii BBSome is an IFT
1048 cargo required for export of specific signaling proteins from flagella. J. Cell Biol. 187,
1049 1117–1132. https://doi.org/10.1083/jcb.200909183
1050
1051 Lee, E., Sivan-Loukianova, E., Eberl, D.F., Kernan, M.J., 2008. An IFT-A protein is required to
1052 delimit functionally distinct zones in mechanosensory cilia. Curr. Biol. CB 18, 1899–
1053 1906. https://doi.org/10.1016/j.cub.2008.11.020
1054
1055 Li, J.B., Gerdes, J.M., Haycraft, C.J., Fan, Y., Teslovich, T.M., May-Simera, H., Li, H., Blacque,
1056 O.E., Li, L., Leitch, C.C., Lewis, R.A., Green, J.S., Parfrey, P.S., Leroux, M.R.,
1057 Davidson, W.S., Beales, P.L., Guay-Woodford, L.M., Yoder, B.K., Stormo, G.D.,
1058 Katsanis, N., Dutcher, S.K., 2004. Comparative Genomics Identifies a Flagellar and
1059 Basal Body Proteome that Includes the BBS5 Human Disease Gene. Cell 117, 541–552.
1060 https://doi.org/10.1016/S0092-8674(04)00450-7
1061
1062 Liem, K.F., Ashe, A., He, M., Satir, P., Moran, J., Beier, D., Wicking, C., Anderson, K.V., 2012.
1063 The IFT-A complex regulates Shh signaling through cilia structure and membrane protein
1064 trafficking. J. Cell Biol. 197, 789–800. https://doi.org/10.1083/jcb.201110049
1065
1066 Loktev, A.V., Zhang, Q., Beck, J.S., Searby, C.C., Scheetz, T.E., Bazan, J.F., Slusarski, D.C.,
1067 Sheffield, V.C., Jackson, P.K., Nachury, M.V., 2008. A BBSome Subunit Links
1068 Ciliogenesis, Microtubule Stability, and Acetylation. Dev. Cell 15, 854–865.
1069 https://doi.org/10.1016/j.devcel.2008.11.001
1070
1071 Mangeol, P., Prevo, B., Peterman, E.J.G., 2016. KymographClear and KymographDirect: two
1072 tools for the automated quantitative analysis of molecular and cellular dynamics using
1073 kymographs. Mol. Biol. Cell 27, 1948–1957. https://doi.org/10.1091/mbc.E15-06-0404
1074
1075 Mick, D.U., Rodrigues, R.B., Leib, R.D., Adams, C.M., Chien, A.S., Gygi, S.P., Nachury, M.V.,
1076 2015. Proteomics of Primary Cilia by Proximity Labeling. Dev. Cell 35, 497–512.

1077 https://doi.org/10.1016/j.devcel.2015.10.015
1078
1079 Miryounesi, M., Bahari, S., Salehpour, S., Alipour, N., Ghafouri-Fard, S., 2019. ELMO Domain
1080 Containing 1 (ELMOD1) Gene Mutation Is Associated with Mental Retardation and
1081 Autism Spectrum Disorder. J. Mol. Neurosci. 69, 312–315.
1082 https://doi.org/10.1007/s12031-019-01359-z
1083
1084 Mukhopadhyay, S., Wen, X., Chih, B., Nelson, C.D., Lane, W.S., Scales, S.J., Jackson, P.K.,
1085 2010. TULP3 bridges the IFT-A complex and membrane phosphoinositides to promote
1086 trafficking of G protein-coupled receptors into primary cilia. Genes Dev. 24, 2180–2193.
1087 https://doi.org/10.1101/gad.1966210
1088
1089 Nachury, M.V., 2014. How do cilia organize signalling cascades? Philos. Trans. R. Soc. Lond.
1090 B. Biol. Sci. 369. https://doi.org/10.1098/rstb.2013.0465
1091
1092 Nachury, M.V., Loktev, A.V., Zhang, Q., Westlake, C.J., Peränen, J., Merdes, A., Slusarski,
1093 D.C., Scheller, R.H., Bazan, J.F., Sheffield, V.C., Jackson, P.K., 2007. A Core Complex
1094 of BBS Proteins Cooperates with the GTPase Rab8 to Promote Ciliary Membrane
1095 Biogenesis. Cell 129, 1201–1213. https://doi.org/10.1016/j.cell.2007.03.053
1096
1097 Nozaki, S., Castro Araya, R.F., Katoh, Y., Nakayama, K., 2019. Requirement of IFT-B–BBSome
1098 complex interaction in export of GPR161 from cilia. Biol. Open 8, bio043786.
1099 https://doi.org/10.1242/bio.043786
1100
1101 Ou, G., E. Blacque, O., Snow, J.J., Leroux, M.R., Scholey, J.M., 2005. Functional coordination
1102 of intraflagellar transport motors. Nature 436, 583–587.
1103 https://doi.org/10.1038/nature03818
1104
1105 Ou, G., Koga, M., Blacque, O.E., Murayama, T., Ohshima, Y., Schafer, J.C., Li, C., Yoder, B.K.,
1106 Leroux, M.R., Scholey, J.M., 2007. Sensory Ciliogenesis in *Caenorhabditis elegans* :
1107 Assignment of IFT Components into Distinct Modules Based on Transport and
1108 Phenotypic Profiles. Mol. Biol. Cell 18, 1554–1569. https://doi.org/10.1091/mbc.e06-09-
1109 0805
1110
1111 Patel-King, R.S., Gilberti, R.M., Hom, E.F.Y., King, S.M., 2013. WD60/FAP163 is a dynein
1112 intermediate chain required for retrograde intraflagellar transport in cilia. Mol. Biol. Cell
1113 24, 2668–2677. https://doi.org/10.1091/mbc.E13-05-0266
1114
1115 Pazour, G.J., Dickert, B.L., Vucica, Y., Seeley, E.S., Rosenbaum, J.L., Witman, G.B., Cole,
1116 D.G., 2000. Chlamydomonas IFT88 and its mouse homologue, polycystic kidney disease
1117 gene tg737, are required for assembly of cilia and flagella. J. Cell Biol. 151, 709–718.
1118 https://doi.org/10.1083/jcb.151.3.709
1119
1120 Piasecki, B.P., Burghoorn, J., Swoboda, P., 2010. Regulatory Factor X (RFX)-mediated
1121 transcriptional rewiring of ciliary genes in animals. Proc. Natl. Acad. Sci. 107, 12969–
1122 12974. https://doi.org/10.1073/pnas.0914241107

1123
1124 Prevo, B., Scholey, J.M., Peterman, E.J.G., 2017. Intraflagellar transport: mechanisms of motor
1125 action, cooperation, and cargo delivery. FEBS J. 284, 2905–2931.
1126 https://doi.org/10.1111/febs.14068
1127
1128 Reiter, J.F., Leroux, M.R., 2017. Genes and molecular pathways underpinning ciliopathies. Nat.
1129 Rev. Mol. Cell Biol. 18, 533–547. https://doi.org/10.1038/nrm.2017.60
1130
1131
1132 Rompolas, P., Pedersen, L.B., Patel-King, R.S., King, S.M., 2007. *Chlamydomonas* FAP133 is a
1133 dynein intermediate chain associated with the retrograde intraflagellar transport motor. J.
1134 Cell Sci. 120, 3653–3665. https://doi.org/10.1242/jcs.012773
1135
1136 Rosenbaum, J.L., Witman, G.B., 2002. Intraflagellar transport. Nat. Rev. Mol. Cell Biol. 3, 813–
1137 825. https://doi.org/10.1038/nrm952
1138
1139 Ruiz García, S., Deprez, M., Lebrigand, K., Cavard, A., Paquet, A., Arguel, M.-J., Magnone, V.,
1140 Truchi, M., Caballero, I., Leroy, S., Marquette, C.-H., Marcet, B., Barbry, P., Zaragosi,
1141 L.-E., 2019. Novel dynamics of human mucociliary differentiation revealed by single-cell
1142 RNA sequencing of nasal epithelial cultures. Development dev.177428.
1143 https://doi.org/10.1242/dev.177428
1144
1145 Satir, P., Christensen, S.T., 2007. Overview of Structure and Function of Mammalian Cilia.
1146 Annu. Rev. Physiol. 69, 377–400.
1147 https://doi.org/10.1146/annurev.physiol.69.040705.141236
1148
1149 Saudi Mendeliome Group, 2015. Comprehensive gene panels provide advantages over clinical
1150 exome sequencing for Mendelian diseases. Genome Biol. 16, 134.
1151 https://doi.org/10.1186/s13059-015-0693-2
1152
1153 Scheidel, N., Blacque, O.E., 2018. Intraflagellar Transport Complex A Genes Differentially
1154 Regulate Cilium Formation and Transition Zone Gating. Curr. Biol. 28, 3279-3287.e2.
1155 https://doi.org/10.1016/j.cub.2018.08.017
1156
1157 Schneider, C.A., Rasband, W.S., Eliceiri, K.W., 2012. NIH Image to ImageJ: 25 years of image
1158 analysis. Nat. Methods 9, 671–675. https://doi.org/10.1038/nmeth.2089
1159
1160 Scholey, J., 2007. The sensory cilia of Caenorhabditis elegans_Revised. WormBook.
1161 https://doi.org/10.1895/wormbook.1.126.2
1162
1163 Schwarz, N., Lane, A., Jovanovic, K., Parfitt, D.A., Aguila, M., Thompson, C.L., da Cruz, L.,
1164 Coffey, P.J., Chapple, J.P., Hardcastle, A.J., Cheetham, M.E., 2017. Arl3 and RP2
1165 regulate the trafficking of ciliary tip kinesins. Hum. Mol. Genet. 26, 2480–2492.
1166 https://doi.org/10.1093/hmg/ddx143
1167
1168 Shaheen, R., Szymanska, K., Basu, B., Patel, N., Ewida, N., Faqeih, E., Al Hashem, A., Derar,

1169 N., Alsharif, H., Aldahmesh, M.A., Alazami, A.M., Hashem, M., Ibrahim, N.,
1170 Abdulwahab, F.M., Sonbul, R., Alkuraya, H., Alnemer, M., Al Tala, S., Al-Husain, M.,
1171 Morsy, H., Seidahmed, M.Z., Meriki, N., Al-Owain, M., AlShahwan, S., Tabarki, B.,
1172 Salih, M.A., Ciliopathy WorkingGroup, Faquih, T., El-Kalioby, M., Ueffing, M., Boldt,
1173 K., Logan, C.V., Parry, D.A., Al Tassan, N., Monies, D., Megarbane, A., Abouelhoda,
1174 M., Halees, A., Johnson, C.A., Alkuraya, F.S., 2016. Characterizing the morbid genome
1175 of ciliopathies. Genome Biol. 17, 242. https://doi.org/10.1186/s13059-016-1099-5
1176
1177 Shamseldin, H.E., Shaheen, R., Ewida, N., Bubshait, D.K., Alkuraya, H., Almardawi, E.,
1178 Howaidi, A., Sabr, Y., Abdalla, E.M., Alfaifi, A.Y., Alghamdi, J.M., Alsagheir, A.,
1179 Alfares, A., Morsy, H., Hussein, M.H., Al-Muhaizea, M.A., Shagrani, M., Al Sabban, E.,
1180 Salih, M.A., Meriki, N., Khan, R., Almugbel, M., Qari, A., Tulba, M., Mahnashi, M.,
1181 Alhazmi, K., Alsalamah, A.K., Nowilaty, S.R., Alhashem, A., Hashem, M., Abdulwahab,
1182 F., Ibrahim, N., Alshidi, T., AlObeid, E., Alenazi, M.M., Alzaidan, H., Rahbeeni, Z., Al-
1183 Owain, M., Sogaty, S., Seidahmed, M.Z., Alkuraya, F.S., 2020. The morbid genome of
1184 ciliopathies: an update. Genet. Med. Off. J. Am. Coll. Med. Genet. 22, 1051–1060.
1185 https://doi.org/10.1038/s41436-020-0761-1
1186
1187 Sigg, M.A., Menchen, T., Lee, C., Johnson, J., Jungnickel, M.K., Choksi, S.P., Garcia, G.,
1188 Busengdal, H., Dougherty, G.W., Pennekamp, P., Werner, C., Rentzsch, F., Florman,
1189 H.M., Krogan, N., Wallingford, J.B., Omran, H., Reiter, J.F., 2017. Evolutionary
1190 Proteomics Uncovers Ancient Associations of Cilia with Signaling Pathways. Dev. Cell
1191 43, 744-762.e11. https://doi.org/10.1016/j.devcel.2017.11.014
1192
1193 Silflow, C.D., Lefebvre, P.A., 2001. Assembly and Motility of Eukaryotic Cilia and Flagella.
1194 Lessons from *Chlamydomonas reinhardtii*. Plant Physiol. 127, 1500–1507.
1195 https://doi.org/10.1104/pp.010807
1196
1197 Sleigh, M.A., 1989. Adaptations of ciliary systems for the propulsion of water and mucus.
1198 Comp. Biochem. Physiol. A Physiol. 94, 359–364. https://doi.org/10.1016/0300-
1199 9629(89)90559-8
1200
1201 SYSCILIA Study Group, van Dam, T.J., Wheway, G., Slaats, G.G., Huynen, M.A., Giles, R.H.,
1202 2013. The SYSCILIA gold standard (SCGSv1) of known ciliary components and its
1203 applications within a systems biology consortium. Cilia 2, 7.
1204 https://doi.org/10.1186/2046-2530-2-7
1205
1206 Thisse, B., Heyer, V., Lux, A., Alunni, V., Degrave, A., Seiliez, I., Kirchner, J., Parkhill, J.-P.,
1207 Thisse, C., 2004. Spatial and Temporal Expression of the Zebrafish Genome by Large-
1208 Scale In Situ Hybridization Screening, in: Methods in Cell Biology. Elsevier, pp. 505–
1209 519. https://doi.org/10.1016/S0091-679X(04)77027-2
1210
1211 Turn, R.E., Linnert, J., Gigante, E.D., Wolfrum, U., Caspary, T., Kahn, R.A., 2021. Roles for
1212 ELMOD2 and Rootletin in ciliogenesis. Mol. Biol. Cell 32, 800–822.
1213 https://doi.org/10.1091/mbc.E20-10-0635
1214

1215 Turan MG, Kantarci H, Temtek SD, Cakici O, Cevik S, Kaplan OI. 2022., Protocol for
1216 determining the average speed and frequency of kinesin and dynein-driven intraflagellar
1217 transport (IFT) in C. elegans. STAR Protoc;3(3):101498. doi:
1218 10.1016/j.xpro.2022.101498.
1219
1220 UK10K Rare Diseases Group, Boldt, K., van Reeuwijk, J., Lu, Q., Koutroumpas, K., Nguyen,
1221 T.-M.T., Texier, Y., van Beersum, S.E.C., Horn, N., Willer, J.R., Mans, D.A., Dougherty,
1222 G., Lamers, I.J.C., Coene, K.L.M., Arts, H.H., Betts, M.J., Beyer, T., Bolat, E.,
1223 Gloeckner, C.J., Haidari, K., Hetterschijt, L., Iaconis, D., Jenkins, D., Klose, F., Knapp,
1224 B., Latour, B., Letteboer, S.J.F., Marcelis, C.L., Mitic, D., Morleo, M., Oud, M.M.,
1225 Riemersma, M., Rix, S., Terhal, P.A., Toedt, G., van Dam, T.J.P., de Vrieze, E.,
1226 Wissinger, Y., Wu, K.M., Apic, G., Beales, P.L., Blacque, O.E., Gibson, T.J., Huynen,
1227 M.A., Katsanis, N., Kremer, H., Omran, H., van Wijk, E., Wolfrum, U., Kepes, F., Davis,
1228 E.E., Franco, B., Giles, R.H., Ueffing, M., Russell, R.B., Roepman, R., 2016. An
1229 organelle-specific protein landscape identifies novel diseases and molecular mechanisms.
1230 Nat. Commun. 7, 11491. https://doi.org/10.1038/ncomms11491
1231
1232 van Dam, T.J.P., Kennedy, J., van der Lee, R., de Vrieze, E., Wunderlich, K.A., Rix, S.,
1233 Dougherty, G.W., Lambacher, N.J., Li, C., Jensen, V.L., Leroux, M.R., Hjeij, R., Horn,
1234 N., Texier, Y., Wissinger, Y., van Reeuwijk, J., Wheway, G., Knapp, B., Scheel, J.F.,
1235 Franco, B., Mans, D.A., van Wijk, E., Képès, F., Slaats, G.G., Toedt, G., Kremer, H.,
1236 Omran, H., Szymanska, K., Koutroumpas, K., Ueffing, M., Nguyen, T.-M.T., Letteboer,
1237 S.J.F., Oud, M.M., van Beersum, S.E.C., Schmidts, M., Beales, P.L., Lu, Q., Giles, R.H.,
1238 Szklarczyk, R., Russell, R.B., Gibson, T.J., Johnson, C.A., Blacque, O.E., Wolfrum, U.,
1239 Boldt, K., Roepman, R., Hernandez-Hernandez, V., Huynen, M.A., 2019. CiliaCarta: An
1240 integrated and validated compendium of ciliary genes. PLOS ONE 14, e0216705.
1241 https://doi.org/10.1371/journal.pone.0216705
1242
1243 Vasquez SSV, van Dam J, Wheway G. 2021. An updated SYSCILIA gold standard (SCGSv2) of
1244 known ciliary genes, revealing the vast progress that has been made in the cilia research
1245 field. Mol Biol Cell. 2021 Dec 1;32(22):br13. doi: 10.1091/mbc.E21-05-0226.
1246
1247 Wei, Q., Xu, Q., Zhang, Y., Li, Y., Zhang, Q., Hu, Z., Harris, P.C., Torres, V.E., Ling, K., Hu, J.,
1248 2013. Transition fibre protein FBF1 is required for the ciliary entry of assembled
1249 intraflagellar transport complexes. Nat. Commun. 4, 2750.
1250 https://doi.org/10.1038/ncomms3750
1251
1252 Wei, Q., Zhang, Y., Li, Y., Zhang, Q., Ling, K., Hu, J., 2012. The BBSome controls IFT
1253 assembly and turnaround in cilia. Nat. Cell Biol. 14, 950–957.
1254 https://doi.org/10.1038/ncb2560
1255
1256 Wheway, G., Genomics England Research Consortium, Mitchison, H.M., 2019. Opportunities
1257 and Challenges for Molecular Understanding of Ciliopathies–The 100,000 Genomes
1258 Project. Front. Genet. 10, 127. https://doi.org/10.3389/fgene.2019.00127
1259
1260 Williams, C.L., Li, C., Kida, K., Inglis, P.N., Mohan, S., Semenec, L., Bialas, N.J., Stupay,

1261 R.M., Chen, N., Blacque, O.E., Yoder, B.K., Leroux, M.R., 2011. MKS and NPHP
1262 modules cooperate to establish basal body/transition zone membrane associations and
1263 ciliary gate function during ciliogenesis. J. Cell Biol. 192, 1023–1041.
1264 https://doi.org/10.1083/jcb.201012116
1265
1266 Williams, C.L., McIntyre, J.C., Norris, S.R., Jenkins, P.M., Zhang, L., Pei, Q., Verhey, K.,
1267 Martens, J.R., 2014. Direct evidence for BBSome-associated intraflagellar transport
1268 reveals distinct properties of native mammalian cilia. Nat. Commun. 5, 5813.
1269 https://doi.org/10.1038/ncomms6813
1270
1271 Wright, K.J., Baye, L.M., Olivier-Mason, A., Mukhopadhyay, S., Sang, L., Kwong, M., Wang,
1272 W., Pretorius, P.R., Sheffield, V.C., Sengupta, P., Slusarski, D.C., Jackson, P.K., 2011.
1273 An ARL3-UNC119-RP2 GTPase cycle targets myristoylated NPHP3 to the primary
1274 cilium. Genes Dev. 25, 2347–2360. https://doi.org/10.1101/gad.173443.111
1275
1276 Xu, Q., Zhang, Y., Wei, Q., Huang, Y., Li, Y., Ling, K., Hu, J., 2015. BBS4 and BBS5 show
1277 functional redundancy in the BBSome to regulate the degradative sorting of ciliary
1278 sensory receptors. Sci. Rep. 5, 11855. https://doi.org/10.1038/srep11855
1279
1280 Xu, W., Jin, M., Hu, R., Wang, H., Zhang, F., Yuan, S., Cao, Y., 2017. The Joubert Syndrome
1281 Protein Inpp5e Controls Ciliogenesis by Regulating Phosphoinositides at the Apical
1282 Membrane. J. Am. Soc. Nephrol. 28, 118–129. https://doi.org/10.1681/ASN.2015080906
1283
1284 Ye, F., Nager, A.R., Nachury, M.V., 2018. BBSome trains remove activated GPCRs from cilia
1285 by enabling passage through the transition zone. J. Cell Biol. 217, 1847–1868.
1286 https://doi.org/10.1083/jcb.201709041